

Copyright

by

Cassie Stuurman

2017

The Thesis Committee for Cassie Stuurman
Certifies that this is the approved version of the following thesis:

**Ridges on Martian Debris-Covered Glaciers:
Deconvolving Structural and Climate Processes**

**Approved by
Supervising Committee:**

Supervisor:

John W Holt

Co-Supervisor:

Joseph S. Levy

Ginny Catania

**Ridges on Martian Debris-Covered Glaciers:
Deconvolving Structural and Climate Processes**

by

Cassie Stuurman, BSc. Earth Sciences

Thesis

Presented to the Faculty of the Graduate School of

The University of Texas at Austin

in Partial Fulfillment

of the Requirements

for the Degree of

MASTER OF SCIENCE IN GEOLOGICAL SCIENCES

The University of Texas at Austin

May 2017

Dedicated to the reader, for bothering

Acknowledgments

I thank the Jackson School of Geosciences and the NASA Mars Data Analysis program for funding this research. I am very thankful to Jack Holt and Joe Levy for being outstanding advisors the entire way through – they are an amazing team and I feel very lucky to have had the opportunity to work with them. I thank Ginny Catania for being an excellent committee member and an excellent professor. Without her instruction this work could never have happened. I am grateful to Liz Logan for very patiently teaching me everything I know about finite element modelling. I am thankful to The Vegan Nom, especially Shay of the North Loop location, for providing me with many cheap breakfast tacos over the course of my Masters. And I am incredibly thankful for Tanya Harrison for being an endless well of encouragement, support, and professional advice.

CASSIE STUURMAN

The University of Texas at Austin

May 2017

Ridges on Martian Debris-Covered Glaciers: Deconvolving Structural and Climate Processes

Cassie Stuurman, MSc. GeoSci
The University of Texas at Austin, 2017

Supervisors: John W. Holt and Joseph S. Levy

Debris-covered glaciers on Earth and Mars often exhibit surface ridges transverse to the flow direction of the glacier. The formation mechanism of these ridges is not well established, but some evidence from terrestrial analogues supports the idea that surface ridges may demarcate climate cycles. It is also possible they are induced by thrust faulting, buckle folding, or other compressional mechanisms. This work aims to differentiate climate-related ridges from thrust fault and buckle folding ridges on Mars through mapping, geometric analysis, and flow modelling. We find that martian glaciers exhibit ridges of a variety of amplitudes and wavelengths. Large ridges on martian debris-covered glaciers cannot be explained by buckle folding given their long arclengths and inconsistent inter-ridge spacing, while some smaller ridges are consistent with the expected arclengths for buckle folds on Mars. The smaller ridges also exhibit highly consistent inter-ridge spacing and morphologies similar to

terrestrial examples of two-layer buckle folds. Flow modelling results suggest that thrust faulting is a possible explanation for ridges on some debris covered glaciers, but thrust faulting diminishes as temperature decreases. We conclude that it some ridges on martian debris-covered glaciers are likely caused by climate variations however the buckle folding hypothesis is plausible for finely spaced ridges.

Contents

Acknowledgments	v
Abstract	vi
List of Tables	x
List of Figures	xi
Chapter 1 Introduction	1
Chapter 2 Methods	10
2.1 Mapping Study	10
2.2 Buckle Folding Geometry Analysis	13
2.3 Modelling Study	16
Chapter 3 Results	22
3.1 Mapping Study	22
3.2 Modelling Study	26
3.3 Buckle Folding Geometry Analysis	31
3.3.1 Tempe Terra Case Study	31
3.3.2 Euripus Mons Case Study	34
3.3.3 Deuteronilus Mensae Case Study	35

Chapter 4 Discussion	38
4.1 Formation Mechanisms for Different Ridge Morphologies	38
4.2 Limitations of the Buckle Folding Analysis	47
Chapter 5 Conclusions	49
References	51

List of Tables

2.1	Model Input Parameters by Regime	21
3.1	Tempe Terra Ridge Measurements	32
3.2	Ridge Measurements for the Mid-Glacier Fine Ridges at Euripus Mons	34
3.3	Ridge Measurements for the Mid-Glacier Coarse Ridges at Euripus Mons	35

List of Figures

1.1	Distribution of Debris-Covered Glaciers on Mars	2
1.2	Cartoon Illustration Different Ridge Formation Hypotheses	4
1.3	Examples of Ridges on Martian Glaciers	9
2.1	Examples of Morphologies on the Euripus Mons Debris-Covered Glacier	11
2.2	Geometry of a Buckle Fold	14
2.3	Martian Model Geometries	18
3.1	Map of Ridges on the Euripus Mons Debris-Covered Glacier	23
3.2	Basal Surface Analysis on the Southern Euripus Mons Glacier	24
3.3	The Relationship between Euripus Mons Morphologies and the Basal Surface	25
3.4	Arolla Glacier Model Results	27
3.5	Negative Basal Curvature Martian Simulation Results	28
3.6	Positive Curvature Martian Simulation Results	29
3.7	Shear Bands in the Compressional Mars Simulation	30
3.8	Buckle Folding Results Summary	32
3.9	Ridges on a Debris-Covered Glacier in Tempe Terra	33
3.10	Mid-Glacier Fine Ridges at Euripus Mons	35
3.11	A Deuteronilus Mensae Debris-Covered Glacier	36

4.1	Pahoehoe Buckle Folds and the Euripus Mons Ridges	40
4.2	Conceptual Model for Climate-Related Ridge Development	45
4.3	Examples of Potential Climate-Related Ridges	46
4.4	Detrended Elevation Profile over Tempe Terra Ridges	47

Chapter 1

Introduction

Debris-covered glaciers are the most substantial deposit of midlatitudinal water ice on Mars with a volume of $2.63 \times 10^5 \text{ km}^3$ [Levy et al., 2014]. They take the form of lobate debris aprons, lineated valley fill, concentric crater fill, and viscous flow features in the northern and southern hemispheres between $30\text{-}50^\circ$ latitude (Figure 1.1). Surface ridges transverse to the direction of flow are commonly observed on martian debris-covered glaciers [Chuang and Crown, 2005, Levy et al., 2007, Squyres, 1978]. The ridges tend to be arcuate, regularly spaced, and in some cases follow the shape of the glacier headwall (Figure 1.3). This study aims to examine a putative relationship between surface ridges on martian debris-covered glaciers and paleoclimate cycles.

The earliest Viking studies of martian debris-covered glaciers denoted the features “lobate debris aprons” (LDA) [Squyres, 1978, 1979]. They were thought to be composed of predominantly lithic material eroded from valley walls with an interstitial water ice component diffused from the atmosphere [Lucchitta, 1984, Squyres, 1978]. Comparisons were drawn to terrestrial rock glaciers [Squyres, 1978] and gelifluction features [Carr and Schaber, 1977]. Authors completed numerous studies examining their stratigraphy and surface structures, including some investiga-

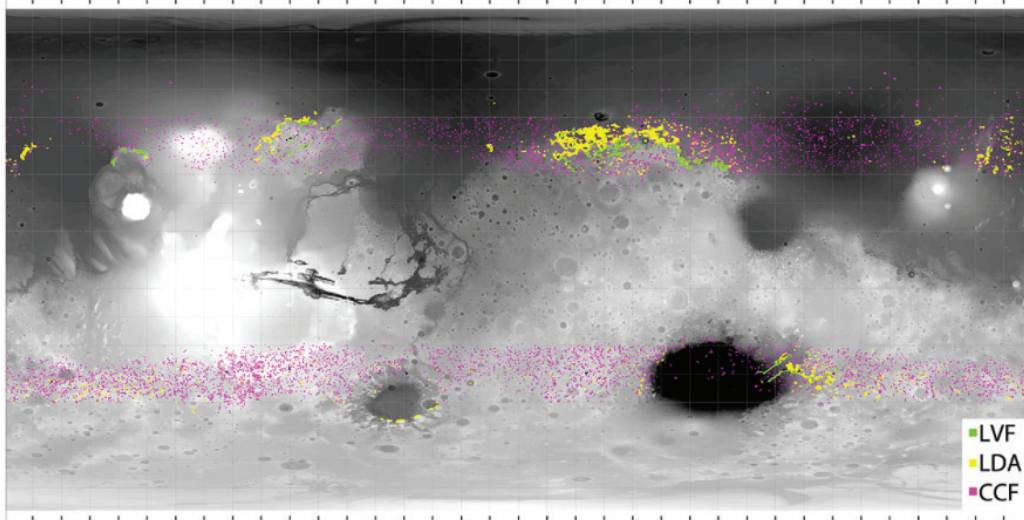


Figure 1.1: A map from Levy et al. [2014] showing the distribution of debris-covered glaciers on Mars. They are concentrated in the midlatitudes of both the northern and southern hemispheres.

tions into transverse ridges: Squyres [1978] examined surface lineations on fretted terrain LDAs and suggested the transverse ridges were the result of compression inducing differential flow velocities; Squyres and Carr [1986] examined latitudinal trends in creep morphology, making some links to rheological changes with temperature; Pierce and Crown [2003] identified that LDAs in eastern Hellas likely formed by multiple large debris emplacement events followed by viscous flow and surface degradation; Chuang and Crown [2005] noted that transverse ridges on LDAs run parallel the curvature of massif walls and linked this to possible variable debris input through time.

More recent studies of LDA features using the SHallow RADar (SHARAD) instrument on Mars Reconnaissance Orbiter [Seu et al., 2007] have shown they are not rock glaciers but debris-covered glaciers composed of clean ice overlain by a thin (1-10 m) layer of debris [Holt et al., 2008, Plaut et al., 2009]. Features analogous to transverse ridges observed on martian LDAs are commonly found on terrestrial

debris-covered glaciers [Florentine et al., 2014, Frehner et al., 2015, Mackay and Marchant, 2017, Mackay et al., 2014, Wahrhaftig and Cox, 1959]. Several hypotheses for transverse ridge development exist. Some authors have proposed they may be shortening features, like compressional ridges observed on clean-ice glaciers [Kääb and Weber, 2004, Pierce and Crown, 2003]. Another interpretation invokes aeolian modification based on their morphological similarity to dunes [Pierce and Crown, 2003]. Others suggest that the viscosity differential at the debris-ice interface drives buckle-folding, a phenomenon that can produce ridge-furrow morphology with highly regular wavelengths [Frehner et al., 2015, Loewenherz et al., 1989]. Explanations involving variable debris input have also been proposed [Chuang and Crown, 2005]. Authors have also explored the possibility that changes in rheological properties or bedrock topography could produce ridges [Grindrod and Fawcett, 2011]. Some authors emphasize the relationship between englacial structure and surface ridges [Florentine et al., 2014, Kirkbride and Deline, 2013, Mackay et al., 2014]. Overall there have been myriad ideas on the formation mechanisms of transverse ridges on debris covered glaciers, but little convergence in the various models for ridge formation.

Terrestrial radar and seismic studies of debris-covered glaciers have shown that surface ridges are frequently associated with internal, up-glacier dipping reflectors. These reflectors have been interpreted as debris bands in some cases [Mackay and Marchant, 2017, Mackay et al., 2014], and as thrust faults in others [Florentine et al., 2014, Fukui et al., 2007].

This study examines four hypotheses for the development of transverse ridges in the context of martian debris-covered glaciers: (1) shortening ridges caused by compression-induced velocity differentials, (2) ridges caused by thrust faults, (3) ridges caused by climate variations, and (4) ridges caused by buckle-folding at viscosity differentials (Figure 1.2).

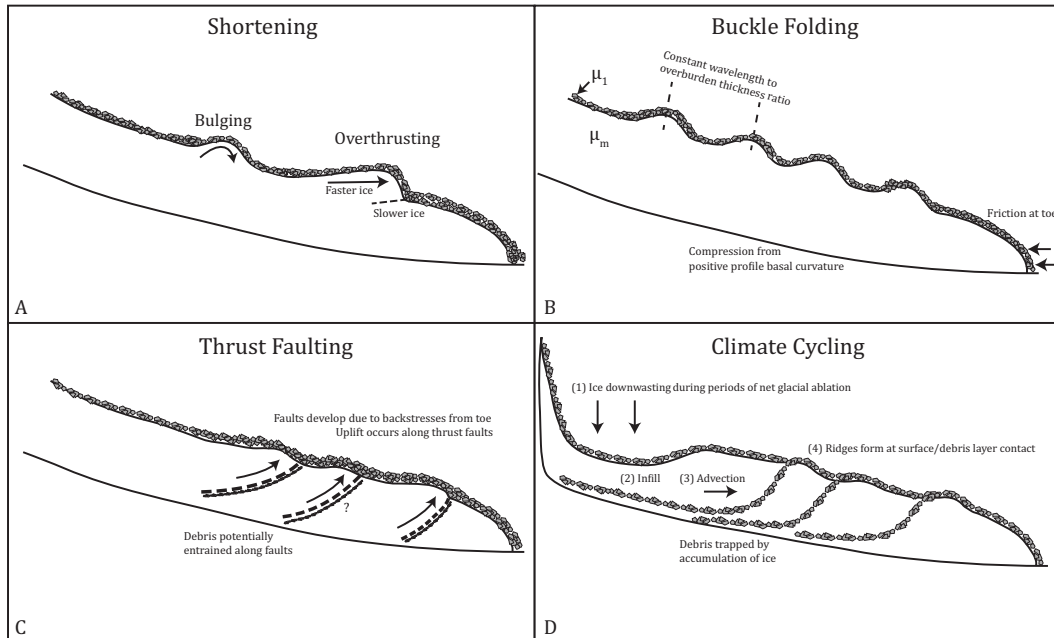


Figure 1.2: **(A)** The shortening hypothesis for ridge development on debris-covered glaciers. Shortening describes a class of compressional ridges that form when ice plastically deforms upwards. In the bulging model, ice moves upwards to compensate for longitudinal compressional forces as the upward surface is not bound. In the overthrusting model, faster ice moves overtop of slower ice down-glacier. Adapted from Kääb and Weber [2004]. **(B)** The buckle folding hypothesis. Ice undergoes upwards ductile deformation as a response to longitudinal compressive stress. In this case, one wavelength of deformation dominates due to the ratio in viscosity between the ice (μ_m) and the debris layer (μ_1). **(C)** Thrust faulting ridges. Compressional back-stresses from the toe induce a series of up-glacier dipping faults. Ice uplifts along the faults forming ridges. Debris may be entrained from below the glacier forming englacial debris bands. **(D)** The climate cycling ridge hypothesis. During periods of net glacial ablation a depression forms near the headwall where the debris layer is thinnest. If the climate moves into a period of net accumulation, debris bands are trapped within the glacier due to infilling of ice near the headwall. The debris bands advect down-glacier and form morphologies where they intersect the glacial surface.

Shortening ridges, for the purpose of this study, is a term used to describe ridges that form in instances where there is a significant decrease in glacier velocity over a short longitudinal distance. This model has been suggested as an explanation for ridges on some martian debris-covered glaciers [Squyres, 1978]. This mechanism results in overthrusting of fast moving, up-glacier ice over slower ice down-glacier. They are distinct from buckle folding ridges in that their morphology is not controlled by viscosity contrasts, and they are distinct from the faulting hypothesis in that movement of ice or debris along fault planes is not needed. Highly regular wavelengths are not explained by this hypothesis and ridges of this type may intersect, truncate, and overlie each other.

The thrust faulting hypothesis is based on the premise that heterogeneous strain, possibly caused by thermal transitions or changes in basal conditions, can induce shear stresses and thrust faults [Nye, 1952]. It has been proposed by some authors that thrust faulting may not be a significant process in cold-based glaciers as the strain rates are too low [Mackay et al., 2014, Moore et al., 2010], but others have invoked basal entrainment of debris along thrust faults as a mechanism explaining debris bands in Antarctic glaciers [Fukui et al., 2007]. It is worth noting that Fukui et al. [2007] also concluded that the internal debris bands were related to the formation of surface ridges. A mechanical model for the development of surface ridges resulting from internal shear in debris-covered glaciers is shown in Springman et al. [2012]. In their model, frictional resistance at the toe of the glacier is compensated by shearing along a series of up-glacier dipping planes and uplift along those planes forming ridges. Florentine et al. [2014] found a series of up-glacier dipping reflectors in ground-penetrating radar data from Lone Peak Rock Glacier, MT, USA. The reflectors were associated with surface ridges and were interpreted as thrust faults. The thrust faulting hypothesis is most often invoked to explain up-glacier dipping heterogeneities in geophysical surveys of debris-covered glaciers. It is defined by the

notion that the stress fields within a glacier are the primary motivating cause for surface ridges, which form as ice is uplifted along fault planes.

The climate hypothesis is related to the faulting model in that it invokes internal, up-glacier dipping heterogeneities as the cause for the development of surface ridges. It differs, however, in its explanation of what the heterogeneities represent. Evidence from the Dry Valleys of Antarctica suggests some ridges on debris-covered glaciers are caused by englacial debris layers formed during periods of glacial decapitation [Mackay et al., 2014]. When a debris-covered glacier ablates, ice is preferentially removed nearest the headwall where the debris layer is thinnest. This results in a spoon-shaped depression near the headwall during periods of net glacial ablation. When the climate transitions into a net accumulation phase, this depression is filled, burying a layer of debris within the glacier. Thus, the climate hypothesis proposes that englacial debris bands demarcate climate cycles. Using a mass balance model based on past solar cycles, seismic and radar reflectors within Mullins glacier, Antarctica have been directly mapped to past obliquity cycles [Mackay and Marchant, 2017]. This result raises the possibility that transverse ridges on debris-covered glaciers may be linked to paleoclimate variations. Martian debris-covered glaciers have potentially captured Amazonian climate variations on the order of 100's of millions of years [Parsons et al., 2011]. Thus, understanding the structure, emplacement, and surface properties of this vast reservoir could potentially lead to a better understanding of past martian ice ages.

Buckle folds form when two adjoining materials with significant rheological contrast flow in a compressive regime [Hudleston, 2015, Hudleston and Treagus, 2010]. It involves a wavelength selection process wherein folds of a certain wavelength develop fastest and dominate the fold pattern [Adamuszek et al., 2013, Frehner et al., 2015]. In this model for ridge development on debris-covered glaciers, the wavelength of ridges would depend on the ratio of the viscosity of the surficial

debris layer and the water ice below it [Frehner et al., 2015, Loewenherz et al., 1989]. The buckle folding hypothesis is different from differential velocity compressional ridges in that the geometry of the ridge is dependent on the viscosity contrast between two materials and occurs in any compressional regime, not only when fast ice flows over slower ice down-glacier. A flow modelling study based on Murtèl rock glacier, Switzerland generated buckle fold ridges using a simple two-layer model of debris overlying clean water ice [Frehner et al., 2015]. The study derived an effective viscosity for the surface debris layer of 9 to 21 times greater than that of the water ice using an analytic relationship describing the expected geometry of ridges for a given ratio in viscosities.

Research on the interior of martian debris-covered glaciers is currently limited by the data available. On Earth it is relatively easy to resolve the potentially climate-related englacial debris bands in radar studies. On Mars, however, there exists abundant imagery for interpreting the surface textures and morphology of martian debris-covered glaciers but our ability to sound their interiors is limited to SHARAD resolutions of ~ 8.5 m/pixel (vertically) and 0.3-1 km (along track), theoretically [Seu et al., 2007]. In practice, resolutions are coarser than the theoretical values due to sidelobes, surface roughness, and processing limitations. Additionally, subsurface reflectors are not observed in all areas where they might be expected [Petersen, 2017], reflectors of a slope greater than 4° will not be observed at all due to along-track coherent summing required to achieve the needed signal-to-noise ratios, and there remain gaps in radar coverage several kilometres wide throughout the midlatitudes. These limitations in our ability to geophysically measure the interior of martian debris-covered glaciers motivates their study using morphological and modelling techniques.

Our modelling study examines two relationships between the internal structure of a glacier and surface ridges. The first aims to characterize the influence of

temperature on thrust faulting in terrestrial glaciers. This will add insight to the debate surrounding basal entrainment versus climate cycling as possible origins for englacial debris bands in cold-based glaciers. In the martian cases, we examine the relationship between basal slope and surface structure to test whether compressive versus extensional flow regimes may influence debris-covered glacier morphology. Some constraints on the input parameters for martian debris-covered glacier modelling already exist and are discussed in detail in Section 2.3.

This study integrates morphology, radar geophysics, modelling, and terrestrial analogue studies to characterize the different types of surface ridges observed on martian debris-covered glaciers. Chapter 2 describes the approaches used in the mapping, modelling, and geometrical analyses in detail. In Chapter 3 we present a map identifying different ridge classes around Euripus Mons. This chapter also includes case studies from Euripus Mons (44.82°S , 104.73°), Deuteronilus Mensae (42.69° , 26.39°), and Tempe Terra (51.17°N , 288.94°) which are used to show that the observed morphology of ridges on martian debris-covered glaciers is not always consistent with the buckle-folding interpretation. Using flow modelling we examine the plausibility of the development of thrust faults within terrestrial cold-based glaciers as well as under martian conditions. In Chapter 4 we present for the first time a mechanism explaining how changes in martian climate could produce surface ridges on debris-covered glaciers, and identify a specific morphology that is most likely to be caused by variations in climate. In Chapter 5 we summarize our main conclusions.

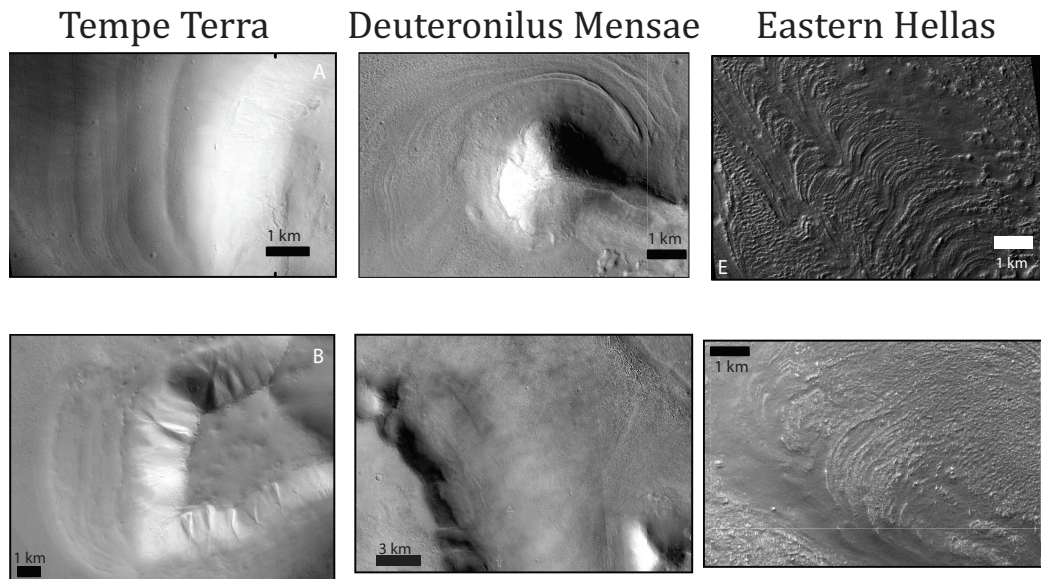


Figure 1.3: Ridges on martian debris-covered glaciers. (A) HiRISE image PSP_009341_2315 (288.8°E , 51.2°N) showing smooth ridges following the shape of the massif wall. This is also the site of the Tempe Terra case study used in the buckle folding analysis. (B) CTX image F02_036531_2303_XN (288.98°E , 51.23°N), smooth ridges running parallel to the shape of the massif wall. (C) CTX image D05_029038_2197_XN (21.22°E , 39.81°N). Smooth arcuate ridges observed on eastern side while northern side has sharply defined truncated ridges. (D) CTX images P13_006160_2252_XN and F05_037701_2249_XN (26.39°E , 42.79°N) showing subtle ridges running parallel to the massif wall. (E) HiRISE image (104.7°W , 44.55°S) showing fine ridges on the northern debris-covered glacier at Euripus Mons. This is the region used for the Euripus Mons Site 1 buckle folding analysis. (F) CTX images B22_018117_XN and D13_032266_1393_XI (103.66°E , 41.54°S). Arcuate ridges near the toe of the glacier. Sometimes truncated.

Chapter 2

Methods

2.1 Mapping Study

A ridge mapping study was completed at Euripus Mons, where the first confirmation of debris-covered glaciers on Mars was undertaken [Holt et al., 2008]. This site was selected for its abundance of SHARAD [Seu et al., 2007], High Resolution Imaging Science Experiment (HiRISE) [McEwen et al., 2007], and ConTeXt (CTX) [Malin et al., 2007] data including CTX digital elevation models (DEMs). It is a well-studied glacier with existing maps for the southern basal surface [Quartini et al., 2011] and detailed rheological estimations based on multiple modelling studies [Parsons and Holt, 2016, Parsons et al., 2011]. The aim of the mapping exercise was to characterize the different ridge morphologies that can be found on martian debris-covered glaciers and to evaluate plausible formation mechanisms, with emphasis on the hypotheses of buckle folding, shortening ridges, climate-related ridges, and thrust faulting ridges.

We mapped lineations based on their tone in imagery and, when possible, their expression in CTX DEMs. We describe four different geomorphic groups of ridges (Figure 2.1). These are:

BC: Broad Continuous. These ridges are broad in scale with a longitudinal

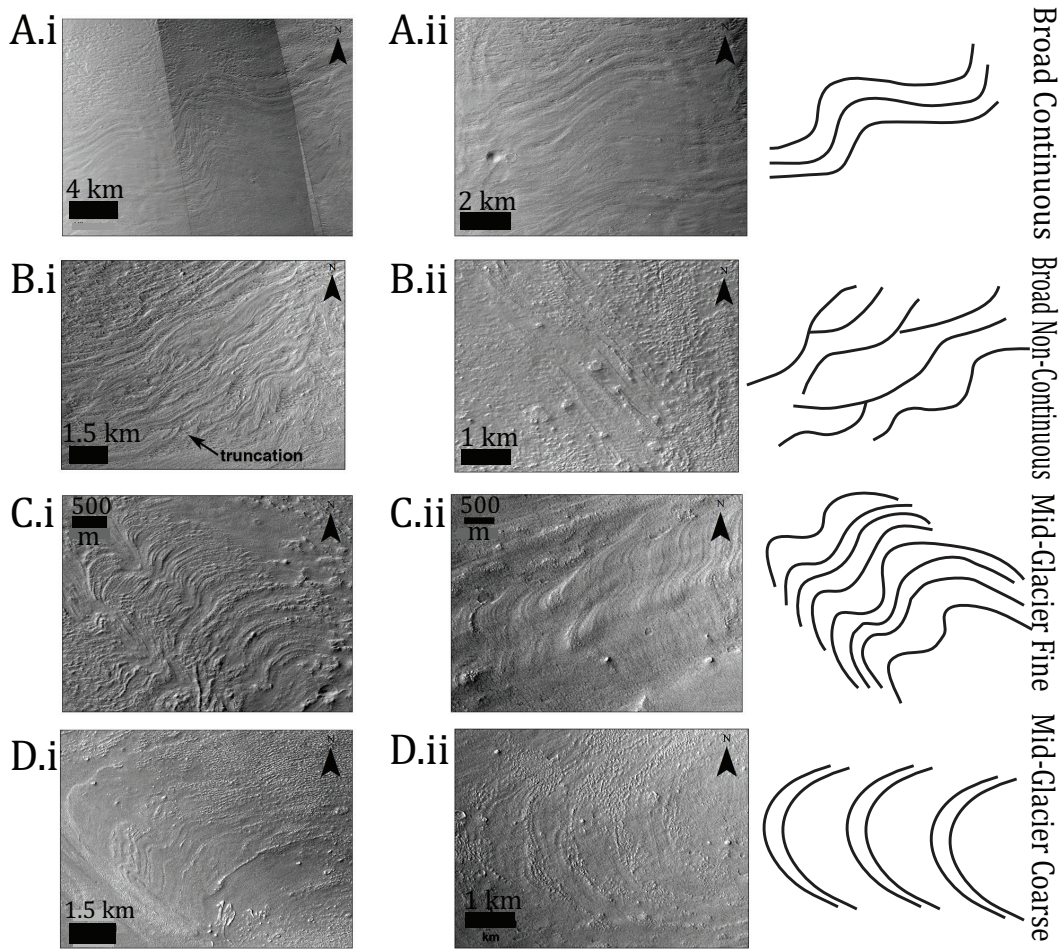


Figure 2.1: Examples of the different ridge morphologies observed around Euripus Mons. **(A.i.)** CTX image mosaic centered on $105.41^{\circ}, -45.155^{\circ}$. **(A.ii.)** CTX image mosaic centered on $105.28^{\circ}, -45.233^{\circ}$. **(B.i.)** CTX image mosaic centered on $104.91^{\circ}, -45.23^{\circ}$ **(B.ii.)** CTX image mosaic centered on $105.01^{\circ}, -44.54^{\circ}$. **(C.i.)** HiRISE image ID ESP_045334_1350. Image centered on $104.73^{\circ}, -44.56^{\circ}$. **(C.ii.)** CTX image B10.013515_1348 centered on $104.33^{\circ}, -45.07^{\circ}$. **(D.i.)** CTX image B10.013515.1348. Image centered on $104.49^{\circ}, -44.57^{\circ}$ **(D.ii.)** Same CTX ID as D.i. Image centered on $104.23^{\circ}, -45.00^{\circ}$. Context for all images provided in Figure 3.1.

inter-ridge spacing ranging from hundreds of metres to 1.5 km and a very long transverse-glacier wavelength (up to 10 km). Their metre-scale vertical amplitude is large enough to be resolved in CTX digital elevation models (DEMs). The ridges appear smooth with rounded peaks and soft transverse curvature. The smoothest material constitutes the peak of the ridge. These ridges consistently run parallel to each other and do not intersect – the inter ridge spacing between any two ridges is relatively consistent, with variations of approximately ± 200 m. They occur in the mid-to-lower glacier and are observed only in the southern portion of the Euripus Mons glacier. These ridges are subparallel the massif headwall (Figure 2.1.A).

BNC: Broad Non-Continuous. These ridges are also broad in scale, but with irregular longitudinal wavelengths on the order of 10^2 metres. Their morphology is more complex, with inconsistent inter-ridge spacing and lengths. The transverse-glacier wavelengths are shorter (10^2 - 10^3 km) and less consistent. They occur in the mid-to-lower parts of the glacier in both the northern and southern portions of the Euripus Mons glacier. In some cases the ridges truncate each other (Figure 2.1.B).

MGF: Mid-Glacier Fine. These ridges are finely spaced with a down-glacier wavelength of tens of metres. The length in the transverse glacier direction is also relatively small, with maximum lengths of kilometre scale. They generally are highly parallel to each other but in rare instances intersect. They occur throughout the length of the glacier, not showing preference for the toe region. (Figure 2.1.C).

MGC: Mid-Glacier Coarse. These ridges also occur along the length of the glacier, but their appearance is coarser than that of the MGF ridges. They have regular longitudinal wavelengths ranging hundreds of metres to 1 km. They are typically shorter in the transverse direction than BC and BNC ridges. They are found in the western and north-western portions of the glacier. The peak of the ridges are typically bouldery and rough-looking. In some cases they occur with MGF ridges in their inter-ridge regions. When MGF are not observed with the MGC ridges the

inter-ridge region is very smooth (Figure 2.1.D).

We then used this catalogue of mapped lineations to examine the relationship between different ridge classes and the basal surface. The aim is to test the influence of basal slope on surface expression – if some ridges tend to occur only in compressional regimes, we hypothesize that they are caused by changes in flow due to basal conditions and not changes in climate. We used a SHARAD-generated subsurface topography map from Quartini et al. [2011] to explore the relationship between surface morphologies and the basal curvature. The map covers a ~ 2100 km² area on the southern side of the Euripus Mons debris-covered glacier. The subsurface elevation, slope, and profile/planform curvatures were sampled along 30 m intervals for the BC and BNC ridges mapped on the southern side the the Euripus Mons debris-covered glacier. Distributions for the population were also obtained by taking samples at 30 m intervals across the entire subsurface map. Statistical hypothesis testing was performed at a confidence level of 95% to look for differences in the basal properties around the BC and BNC morphologies.

2.2 Buckle Folding Geometry Analysis

Because the wavelength of buckle folds depends on the thickness of the folding layer and the ratio in viscosity between the layers involved [Biot, 1961], it is possible to perform a geometrical analysis to investigate whether a ridge could be driven by buckle folding. The relationship governing the wavelength for heterogeneous linear viscous materials is given by

$$\frac{L}{H} = 2\pi \sqrt{\frac{\mu_1}{6\mu_2}} \quad (2.1)$$

where L is the arclength of the fold, h is the thickness of the higher viscosity

layer, μ_1 is the viscosity of the folding layer (in our case, the debris layer), and μ_2 is the viscosity of the matrix (in our case, the water ice layer). In cases where model has been applied to ridges on terrestrial debris-covered glaciers, viscosity ratios were found to range from $10^0 - 10^2$ [Frehner et al., 2015].

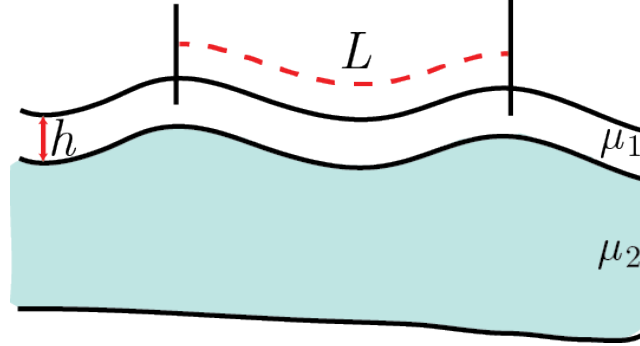


Figure 2.2: Geometry of a buckle fold. The wavelength of ridge is dependent on the ratio in viscosity between the two layers, $\frac{\mu_1}{\mu_2}$, and the thickness of the higher viscosity layer h . In our case the upper layer is the overburden and the lower layer is glacial ice.

While numerous experimental and modelling studies have examined the changes in water ice viscosity under different pressures and temperatures, the viscosity of the debris layer is harder to characterize. We do know that as conditions approach the extremely low temperatures and driving stresses of Mars debris-covered glaciers the water ice viscosity increases dramatically and is estimated to be $10^{17} - 10^{20}$ Pa·s based on experimental and modelling studies [Goldsby and Kohlstedt, 2001, Parsons and Holt, 2016, Parsons et al., 2011]. The simplest models of dense granular flow describe the constitutive relationship governing stress and strain as

$$\tau = P\mu(I)$$

$$\phi = \phi(i)$$

where τ is the shear stress σ_{xz} , P is the normal stress σ_{zz} , ϕ is the volume fraction of the granular material, and I is a dimensionless parameter called the inertial number:

$$I = \frac{\dot{\gamma}d}{\sqrt{P/\rho_p}}$$

where $\dot{\gamma}$ is the strain rate, d is the thickness of the granular layer, and ρ_p is the density given the confinement pressure P . The effective viscosity is then

$$\eta_{eff} = \frac{\mu(I)P}{|\dot{\gamma}|}$$

This assumes the granular material is an incompressible, non-Newtonian fluid. By this relation the viscosity increases linearly with the friction coefficient $\mu(I)$ and the pressure P . A comprehensive analysis of martian debris layer rheology would require detailed measurements of its strain rates, slope angles, thickness, density, grain size, and fluid fraction (if any). Thus, such characterization is impossible with the data currently available. We can predict, however, that the friction coefficient describing inter-granular behaviour will remain approximately the same as for Earth (as it is based solely on the frictional behaviour of rock). The normal stresses, P , acting on the debris layer are $\sim 60\%$ lower than the terrestrial case due to the difference in gravity. Thus, it is reasonable to assume that the viscosity of the debris layer will likely be lower than that of a similar layer on Earth.

Because we expect the water ice viscosity, μ_2 , to be higher and the debris layer viscosity μ_1 to be the same or lower, the viscosity ratios observed on terrestrial debris-covered glaciers can be treated as an upper bound for buckle folds on Mars. By this model, we expect the viscosity *ratio* $\frac{\mu_1}{\mu_2}$ for buckle folds on martian debris

covered glaciers to be a maximum of 10^2 using order-of-magnitude results from terrestrial debris-covered glaciers [Frehner et al., 2015].

The buckle folding geometry analysis tests three case studies, each in a different region with a different ridge morphology, to determine whether the buckle folding relationship produces reasonable viscosity ratios compared to the terrestrial case. HiRISE DEMs were used for the studies in Tempe Terra and Deuteronilus Mensae. At Euripus Mons, no DEM was available, but because the ridge relief appears to be very small we expect the difference between geographic distance and arclength to be negligible. We support this assumption with a surface distance and arclength comparison in the Tempe Terra case study. Because there are multiple types of ridge morphologies found at Euripus Mons we split the analysis into two case studies. For the Site 1 analysis we chose 5 tightly-spaced MGF ridges in the mid-glacier region that exhibited the least amount of apparent degradation and mantling. For the Site 2 analysis we selected 5 consistently-spaced MGC ridges that do not have MGF ridges inbetween them.

Our models do not account for input mass in the glacier accumulation area. Because we are interested in deformation around mid-glacier heterogeneities and the implications for the surface morphology, it is reasonable to exclude input mass near the headwall. The influence of dust content on flow was accounted for using the methods of Parsons and Holt [2016], Parsons et al. [2011].

2.3 Modelling Study

We used the DynEarthSol3D (DES3D) deformation model to examine how the internal structure of a glacier may relate to its surface morphologies [Ta et al., 2015]. The motivating question for our terrestrial simulations was whether it is possible to develop thrust faults in cold-based debris covered glaciers. In the martian simulations, the primary goal was to examine the effect of changing basal slope on surface

morphologies. DES3D is a full Stokes, Lagrangian finite-element model with 2D and 3D capabilities for the simulation of dynamic continuous media. It was chosen for this problem for its capability to model multi-phase bodies with complicated boundaries, such as debris layers overlying glacial ice [Logan et al., in prep., Ta et al., 2015]. It solves the momentum balance and heat equations using unstructured, adaptive meshes to represent deformation. We used some results from Parsons and Holt [2016], Parsons et al. [2011] as input for the model, outlined in Table 2.1.

We ran our simulations in one of three regimes: Warm, Cold, and Mars (Table 2.1). In the martian case the gravity, flow law, activation energies, and range of allowed viscosities were also changed to account for the changes in water ice’s rheological behaviour. Parameters for the martian case were chosen from a variety of experimental and modelling studies, delineated in Table 2.1. Two main geometries were used to simulate martian glacial flow: one in a compressive, positive basal curvature regime and another in an extensional, negative basal curvature regime (Figure 2.3). The aim is to evaluate the controls that basal slope has on internal structure and surface morphologies. DES3D allows different materials to be modelled by different elastic and viscoelastic behaviour. In terrestrial cases we modelled the debris layer as a Mohr-Coulomb elastoplastic medium and the ice as a Maxwell material. In the martian simulations, the debris layer was modelled as a Maxwell material due to computational limitations that make the elastoplastic simulation prohibitively slow over long model timescales.

The viscosity is calculated by DynEarthSol as

$$\mu = \frac{1}{4} A^{-1/n} \dot{\epsilon}^{(1-n)/n}$$

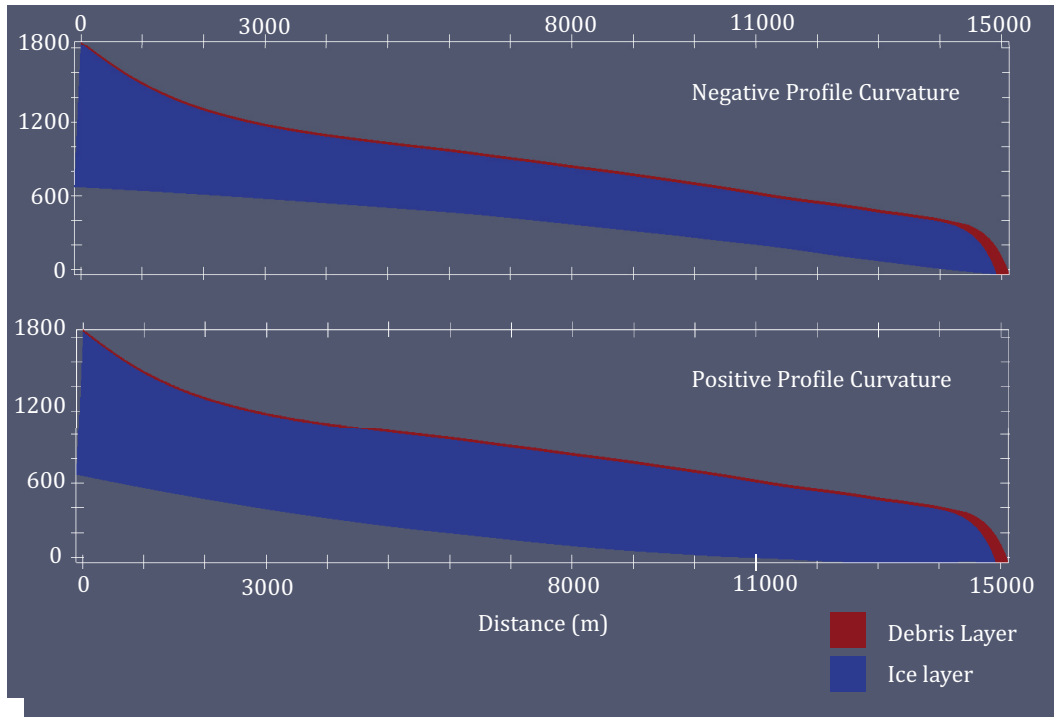


Figure 2.3: Martian model initial geometries with a vertical exaggeration of 2x. The geometry of the upper model was based on MOLA elevation for the surface and SHARAD interpretation from Quartini et al. [2011] for the subsurface. The geometry of the lower model uses MOLA elevation for the surface and the same SHARAD-derived subsurface with a parabola subtracted from the interpretation, forming a compressive basal surface that decreases in slope along the profile of the glacier.

and the flow law as

$$\dot{\epsilon} = A\tau^n d^{-p}$$

where $A = A'e^{-Q/RT-\phi b}$, τ is the stress, ρ is the material density, h is the ice thickness, x is the longitudinal distance, z is the vertical distance, g is the gravitational acceleration, A is a temperature-dependent constant, A' is the temperature-independent flow coefficient, n is the flow exponent, θ is the surface slope, d is the ice grain size, p is the grain size exponent, $b = 2.9$ is a constant [Mangold et al., 2002, Parsons et al., 2011], $\dot{\epsilon}$ is the strain rate, Q is the activation energy, R is the gas constant, ϕ is the dust fraction, and T is temperature.

Because the conditions of Mars are so different from those of Earth, we use different rheological parameters in the martian and terrestrial simulations. Goldsby and Kohlstedt [2001] describe the ways that polycrystalline ice may deform given different temperature, stress, and grain size regimes. For the terrestrial models we used a flow parameter of $n=3$, a dust fraction of $\phi=0$, and $p=0$ as this flow regime is not sensitive to grain size. To simulate martian conditions, we ran models in the grain size-sensitive (GSS, $n=2$) creep regimes. This is consistent with the approach of Parsons et al. [2011]. We selected an ice grain size of 5 mm for our models, which corresponds to a dust fraction of 8% as defined by the relationship between grain-boundary pinning and volumetric dust fraction as constrained by SHARAD [Parsons and Holt, 2016]:

$$\phi = \left[\frac{4\mu\text{m}}{d} \frac{r_d}{1\mu\text{m}} \right]$$

Where r_d is the dust fraction radius, chosen as 100 μm based on Parsons and Holt [2016]. Model runs were designed to determine how the relationship between

internal deformation and surface morphology changes as conditions approach those of martian glaciers.

The geometry used for the terrestrial simulations was based on Arolla glacier in Switzerland, a benchmark glacier for modelling studies [Pattyn et al., 2008]. The debris layer began 500 m from the glacier’s headwall and increased linearly in thickness from 1 - 20 m (Figure 3.4). The geometry for the martian case used Mars Orbiter Laser Altimetry (MOLA) topography [Smith et al., 2001] for the surface and SHARAD interpretations for the subsurface profile [Quartini et al., 2011]. Martian debris layer thickness was programmed into the model as a surface layer 2-15 m thick that increases linearly in thickness along the longitudinal glacier axis. To increase driving stresses and also to aid in comparison to observations, the length of the profile was reduced by two and the thickness of the glacier doubled. This results in a roughly mass-conserved geometry for the flow model. Simulations were deemed realistic by comparison of timescales for flow required to reach the current-day lengths. Estimates on the age of LDA deposits at Euripus Mons range from a minimum of 40 million years found by crater counting studies [Head et al., 2005] to a maximum of 1 Gyr based on analyses of craters filled with glacial ice [Berman et al., 2015]. As this study is primarily concerned with how internal deformation influences the evolution of surface structures (and not pinpointing exact rheological properties of the ice), precision regarding the exact timescale of flow is not critically important. Thus, we accept a simulation as “physical” if it reaches the expected surface velocities from Parsons and Holt [2016] and Pattyn et al. [2008] (See discussion in Chapter 4).

Parameter	Warm Regime	Cold Regime	Martian Regime
Temperature T (K)	260 - 273	247 - 260	205 ^a
Gravity g ($\frac{m}{s^2}$)	9.8	9.8	3.7
Activation Energy Q (kJ mol ⁻¹)	50	50	49 ^b
Flow Exponent n	3	3	2 ^c
Density ρ ($\frac{kg}{m^3}$)	911	911	925
Flow Coefficient A' (Pa ⁻² s ⁻¹)	3×10^{-3}	3×10^{-3}	5×10^{-15}
Ice Grain Size d (mm)			5
Grain Size Exponent p			1.4
^a Parsons et al. [2011]			
^b Goldsby and Kohlstedt [1997]			
^c Goldsby and Kohlstedt [2001]			

Table 2.1: Table of input parameters for each model regime.

Chapter 3

Results

3.1 Mapping Study

Morphologies mapped in Figure 3.1 exhibit a heterogeneous distribution across the surface of the debris-covered glacier. BC (broad continuous) and BNC (broad non-continuous) ridges tend to occur on the southern side of Euripus Mons and also tend to occur together. BNC ridges preferentially occur nearest the toe of the glacier throughout the northern and western sides of Euripus Mons. Towards the south, BNC are found from the mid-glacier to the toe. MGC (mid-glacier coarse) and MGF (mid-glacier fine) ridges are most often found on the western and northern sides of Euripus Mons. MGC ridges sometimes occur with MGF inbetween them, but there are instances where MGC and MGF each occur on their own. Neither MGF nor MGC ridges are found on the southern side of Euripus Mons. Overall the occurrence of each morphology varies from region to region around the massif.

Some statistically significant differences were found in the basal properties around the BC and BNC ridges. Both the BC ($p = 9 \times 10^{-12}$) and BNC ($p = 0.045$) ridges have basal curvature distributions that are different than that of the population at the 5% significance level (Figure 3.3). BNC ridges preferentially occur

where profile curvature is positive. This shows that there is a spatial correlation between BNC ridges and compressional regimes. The BC ridges preferentially occur in areas of negative profile curvature (extensional regimes). The basal slope distributions of the population, BC ridges, and BNC ridges were not normally or lognormally distributed, limiting our options for statistical hypothesis testing. The basal slope values of the BNC ridges are somewhat centered around 1.6, larger than the population mean of 1.4. The basal slope values of the BC ridges do not appear to be centered around any value. The distribution is somewhat uniform from 0.1 to 2 degrees and tails off rapidly to 3.5 degrees.

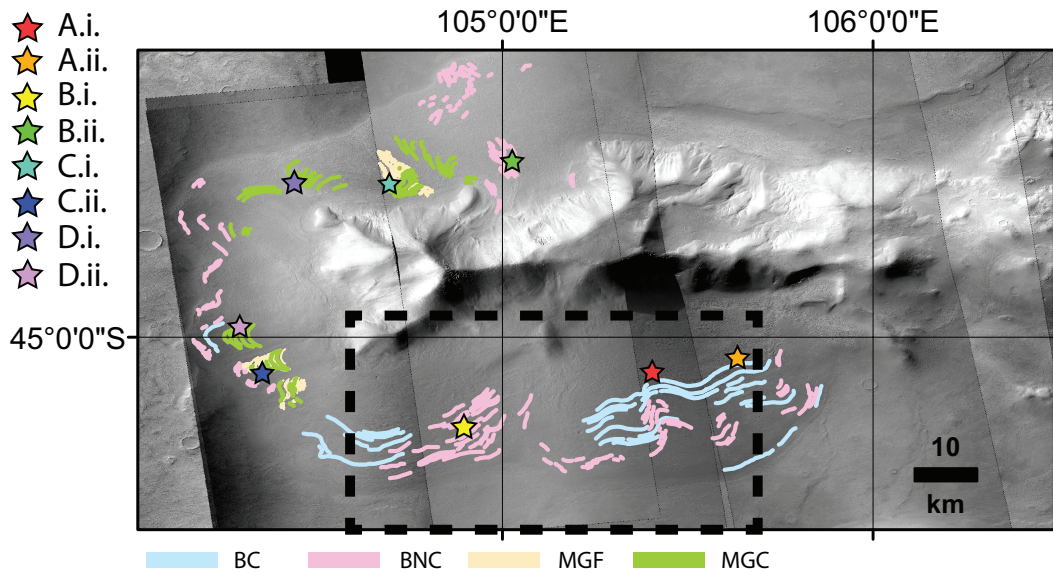


Figure 3.1: Mapping of ridges around Euripus Mons on a CTX mosaic basemap. Locations of example imagery in Figure 2.1 marked by stars. Extent of Figure 3.2 shown by black dotted rectangle.

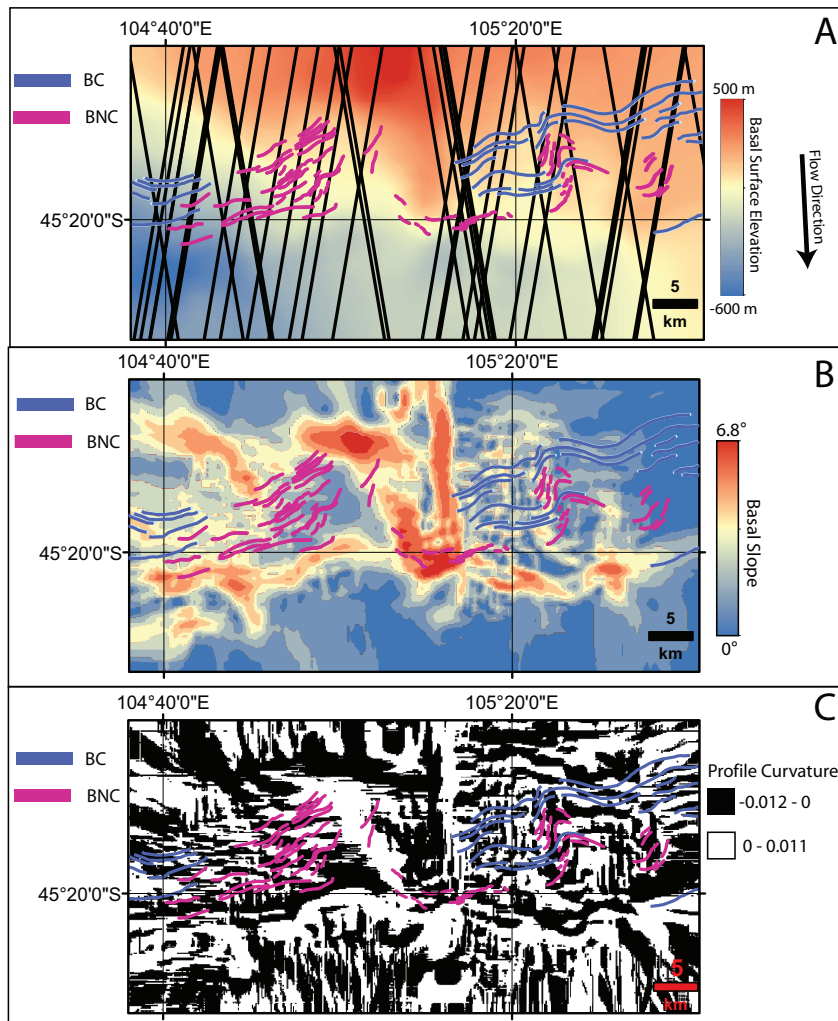


Figure 3.2: Basal surface analysis at the southern Euripus Mons debris-covered glacier. **(A)** Basal surface elevation as derived from SHARAD subsurface reflectors. SHARAD tracks used for the interpolated surface generation are shown by the black lines. Morphological mapping from Figure 3.1 included as blue and pink lineations. Flow direction as inferred from morphology shown by the black arrow. Both BC and BNC ridges do not occur as frequently over the high elevation lobe in the center of the image. **(B)** Map of the basal slope as computed by ArcMap using the interpolated surface in (A). The BNC ridges appear to cluster in areas where there is a decreasing slope along the flow profile. **(C)** Map of the profile curvature, computed by ArcMap. Positive curvature is shown in white and negative curvature in black. The BNC ridges preferentially occur in areas of positive profile curvature.

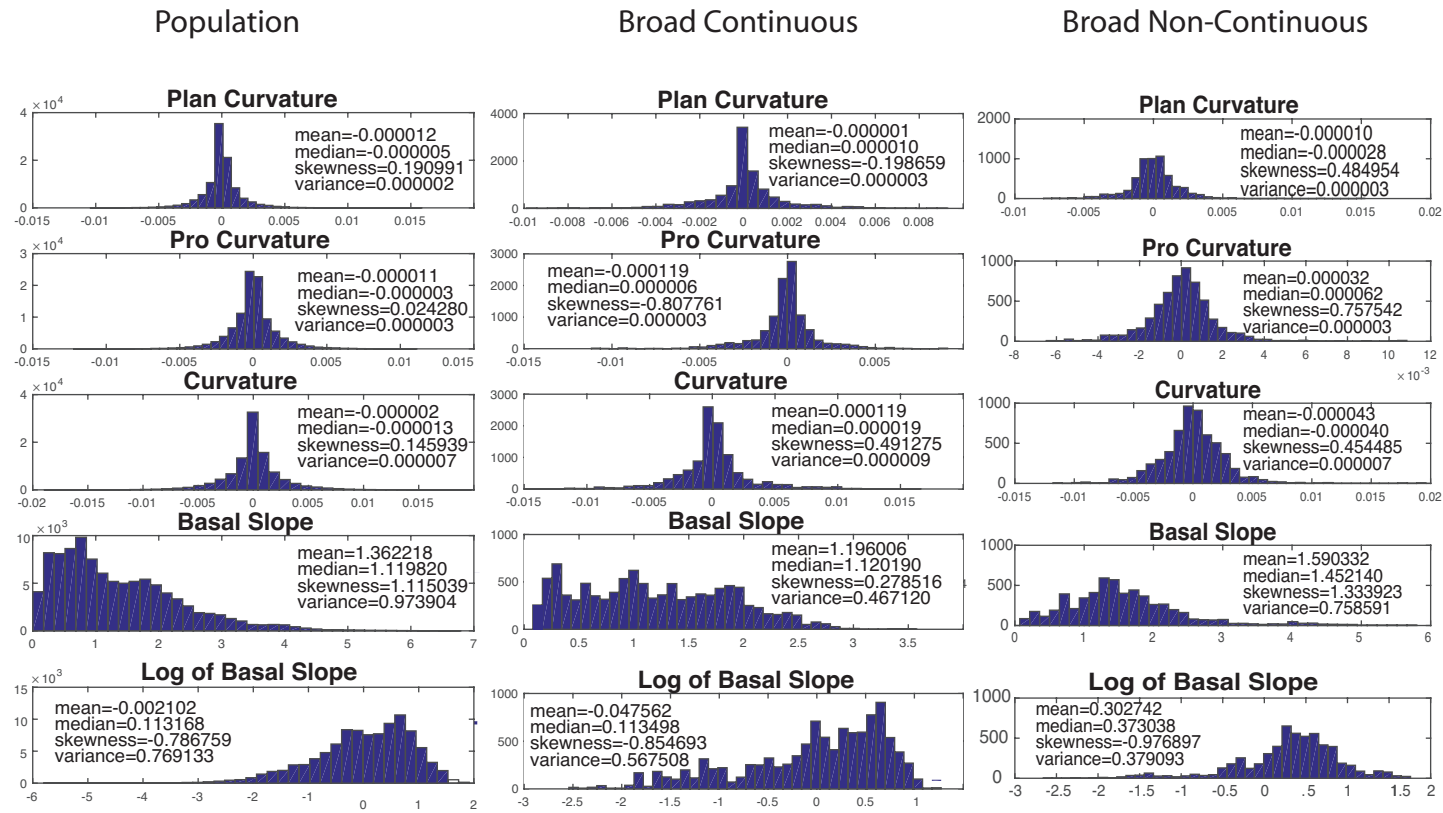


Figure 3.3: The relationship between different mapped morphologies and the basal topography below the debris-covered glacier complex at southern Euripus Mons.

3.2 Modelling Study

Model velocities observed in the terrestrial and martian cases were both comparable to existing values in the literature. The maximum velocity in our martian models reached 3.5 m/Myr, roughly comparable to the 10 m/Myr expected from Parsons et al. [2011]. Our Arolla models reached maximum velocities of 15.77 m/year, highly comparable to observed maximum velocities of 15 m/year [Hubbard et al., 1998].

Results from the terrestrial simulations show diminishing internal structure with decreasing temperature. In the temperate (“warm”) case (Table 2.1), bands of high (0.89) shear strain sometimes developed arcing from a high shear zone in the mid to lower glacier up to the surface (Figure 3.4). Where these shear bands intersect the surface, ridges develop. Ridge amplitudes range from 2-20 m and are of inconsistent wavelengths ranging 10-200 m. Shear bands occurred most frequently in regions of positive basal curvature, namely $x=1300-1600$ and $x=1800-2000$. These regions also have the highest amounts of shear strain in the lower glacier and the largest surface velocities. These linear, up-glacier dipping bands of high shear strain were not observed in the cold-based case. The maximum strain rates observed in the cold case were $5.0 \times 10^{-13} \frac{1}{s}$, an order of magnitude smaller than the maximum strain rate in the warm case ($2.0 \times 10^{-12} \frac{1}{s}$).

If the terrestrial simulations are frozen to the bed, the shear bands develop if the surface velocities are high enough. The cold-based case does not develop shear bands regardless of the boundary condition for the basal surface. The martian simulations show that linear bands of high shear strain can also occur under Mars conditions. They are found throughout the glacier in the compressive regime simulations but only near the headwall and the toe in the extensional regime. In the extensional regime, shear bands are thickest and most dense close to the headwall where there is a dramatic change in glacier thickness.

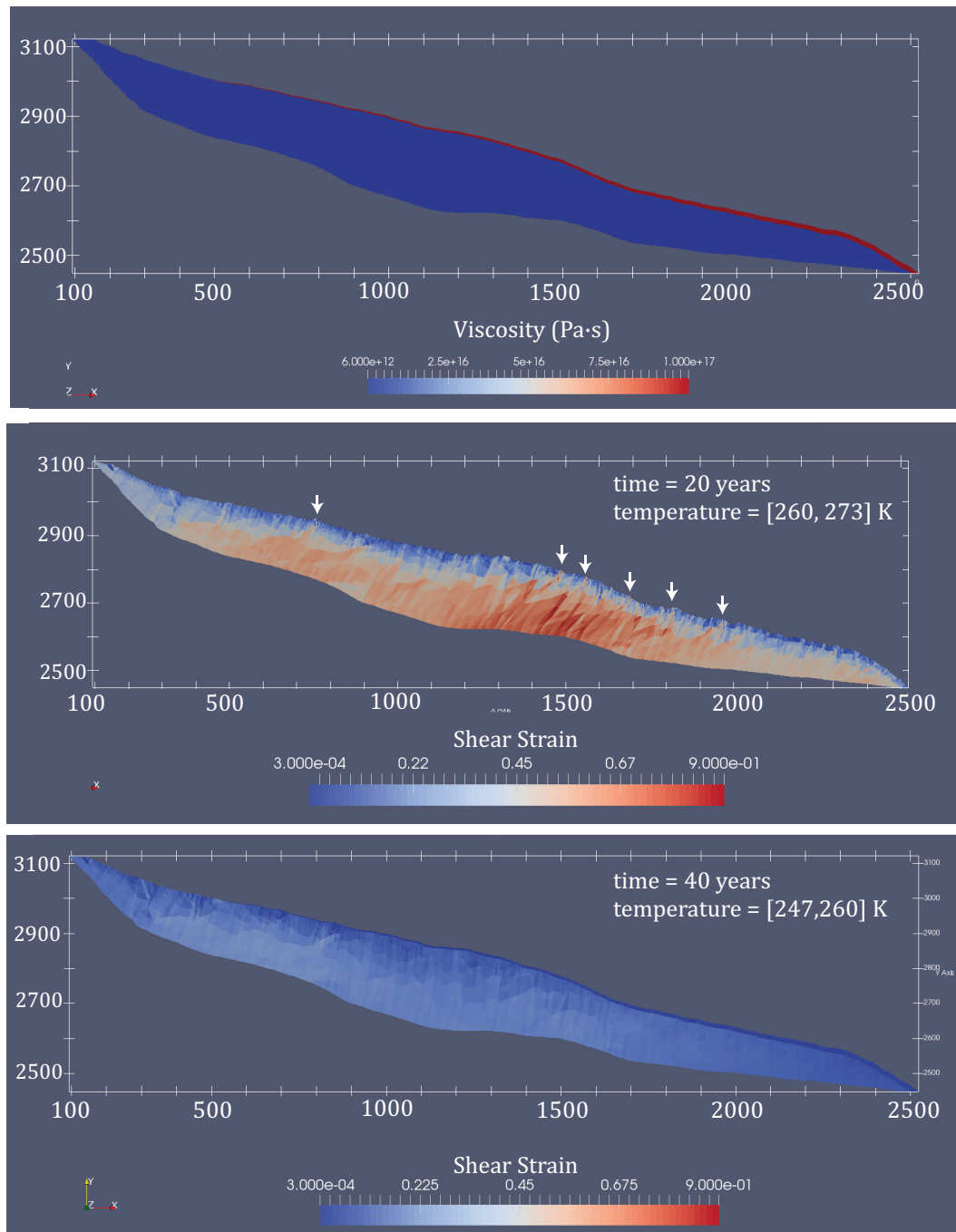


Figure 3.4: **(A)** Initial geometry for the Arolla glacier model runs, vertical exaggeration of 2x. The debris layer increases linearly from 1 - 20 m thickness. **(B)** Shear strain results for the warm debris-covered Arolla case, total model time 20 years. Bands of high shear strain are observed to arc upwards, forming ridges where the intersect the surface. **(C)** Shear strain results for the cold-based case, total model time 40 years. The shear strain is much lower in this temperature regime and the same banding of shear is not observed.

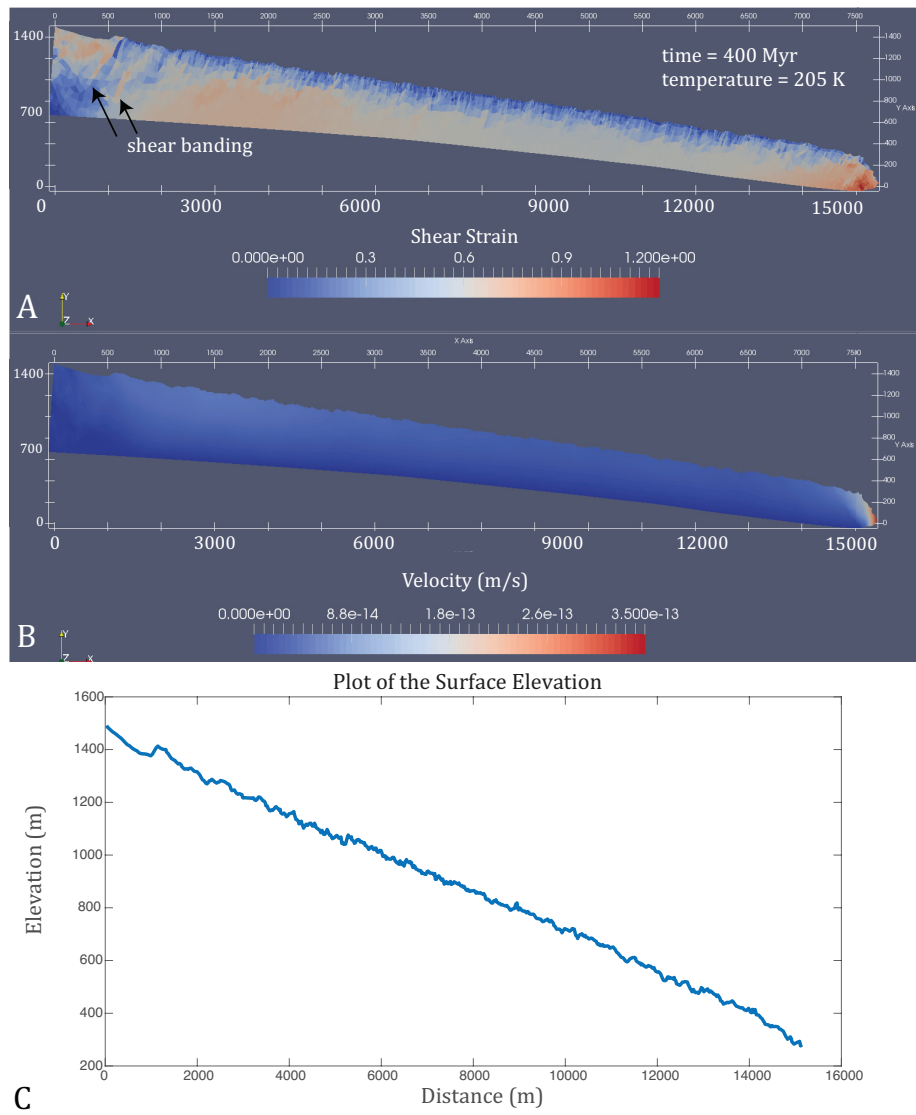


Figure 3.5: Results of the simulation for the negative basal curvature martian glacier. (A) Shear strain showing linear bands of high shear near the headwall. Ridges occur where these bands of high shear strain intersect the surface. (B) The velocity throughout the glacier. Velocities are highest near the headwall where the glacier thickness and driving stresses are highest. (C) Elevation profile for the surface of the glacier.

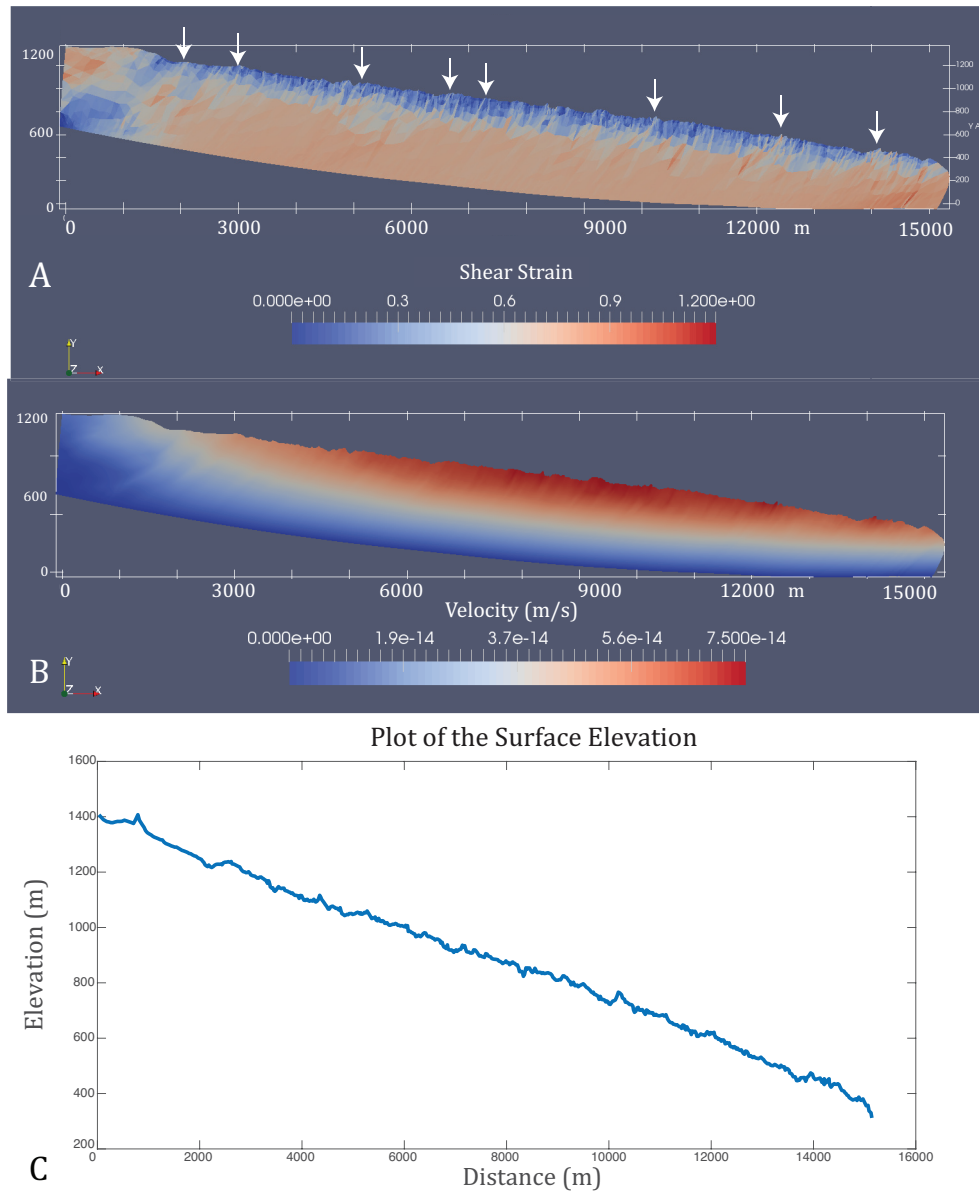


Figure 3.6: Results of the simulation for the positive curvature martian glacier. **(A)** Shear strain results throughout the glacier. White arrows highlight bands of high shear strain intersecting the glacier surface. **(B)** The velocity throughout the glacier. Velocities are highest in the mid to lower glacier. **(C)** Elevation profile for the surface of the glacier.

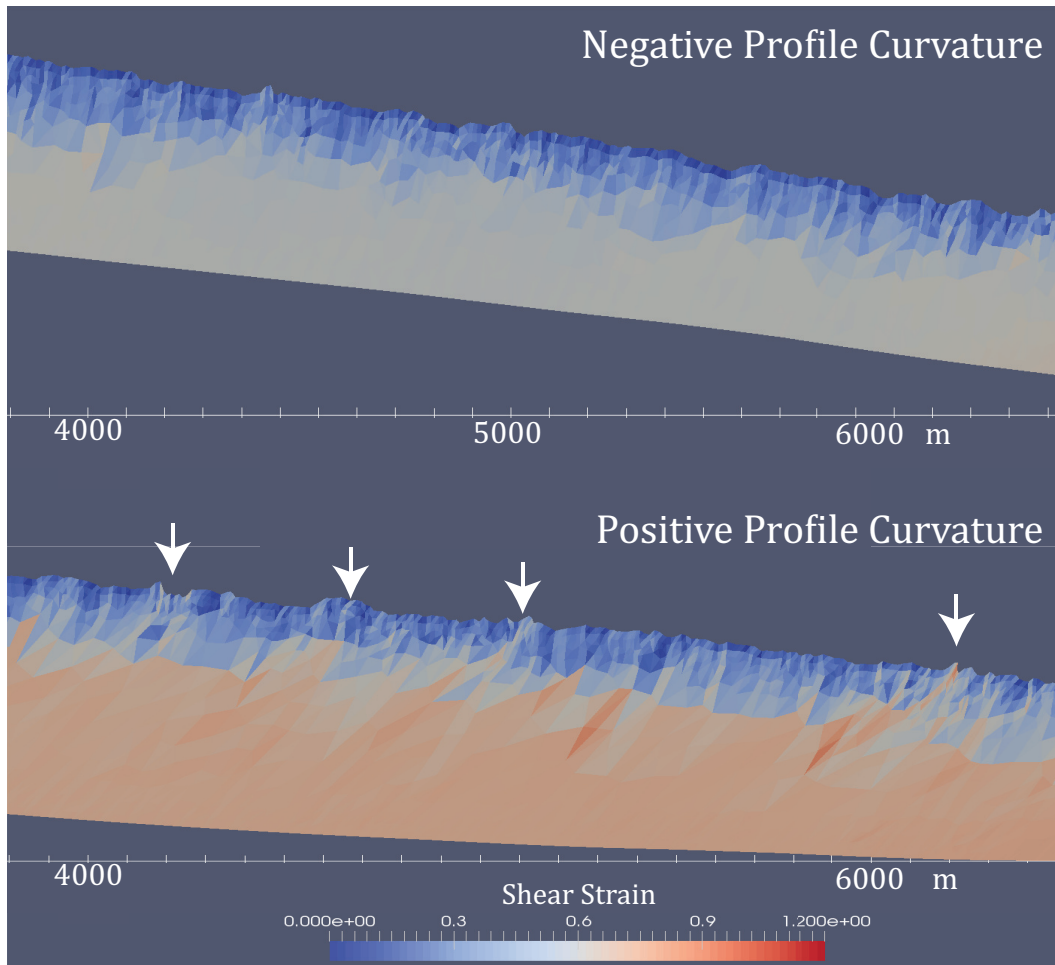


Figure 3.7: Shear banding observed on the surface of compressional regime martian simulations. Arrows point to up-glacier dipping bands of high shear strain in the compressive simulation. The extensional simulation (top) did not produce the same bands of high shear strain in this mid-glacier region.

3.3 Buckle Folding Geometry Analysis

A summary of the buckle folding results is shown in Figure 3.8. We find that the geometry of ridges in the Eastern Hellas case study (104.7°W, 44.55°S) have an estimated viscosity ratio within the expected range for debris-covered glacier buckle folds (for debris layer thicknesses greater than ~ 3 metres). The Deuteronilus Mensae ridges are within the expected range for buckle folding for debris layer thicknesses of ~ 2 to 9 metres. The geometry analysis for ridges in Tempe Terra and western Euripus Mons did not result in reasonable viscosity ratios for any surficial debris layer thickness.

Because we have a range of plausible viscosity ratios and constraints on the surficial debris layer thickness of martian debris-covered glaciers, a maximum possible arclength for buckle folding ridges can be computed. Using the buckle folding relation from Adamuszek et al. [2011]:

$$\begin{aligned}\frac{L}{h} &= 2\pi\sqrt{\frac{\mu_1}{6\mu_2}} \\ &= 2\pi\sqrt{216} \\ &= \sqrt{14}\pi\end{aligned}\tag{3.1}$$

Thus, the maximum ratio of arclength to debris layer thickness plausible for buckle-folding ridges on martian debris-covered glaciers is $\sqrt{14}\pi$, or ~ 12 . The thickness of debris layers overlying martian debris-covered glaciers is constrained to 1-10 m thick Holt et al. [2008], and thus the maximum arclengths that could be explained by buckle folding are 12-120 m long.

3.3.1 Tempe Terra Case Study

The results shown in Table 3.1 yield an average arclength of 586 m. This in turn yields a range of viscosity ratios from 4×10^3 to 5×10^5 . Thus, the viscosity ratio for

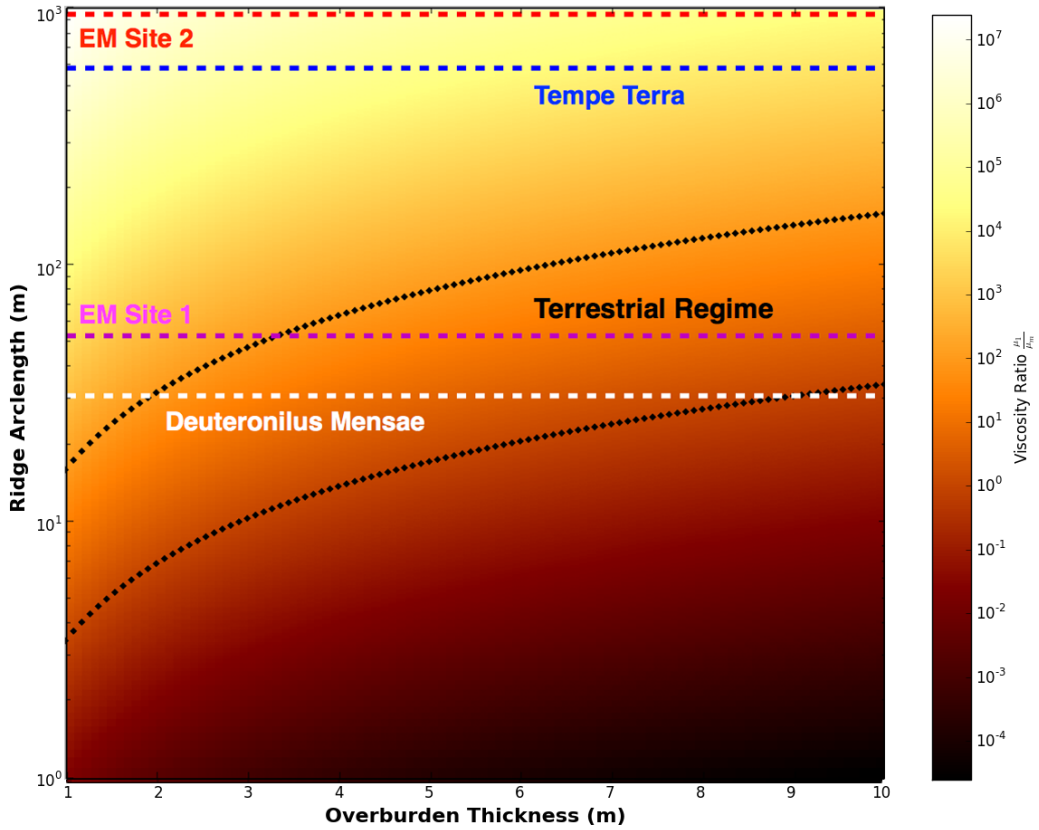


Figure 3.8: Summary of the results from the buckle folding analysis. Buckle folding wavelengths depend on the viscosity ratio between two materials and the thickness of the higher viscosity layer. Given martian ridge wavelengths and debris layer thicknesses, the case study ridges in Eastern Hellas and Deuteronilus Mensae are consistent with the expected viscosity ratios from terrestrial observations. The ridges in the Tempe Terra case study, however, are too large to be explained by buckle folding.

Line segment	Arclength distance	Surface distance	Arclength/surface % difference
A	551 m	549.8 m	0.2%
B	463 m	462.1 m	2%
C	744 m	741.6 m	0.3%

Table 3.1: Measurements corresponding to the different ridges shown in Figure 3.9, the Tempe Terra case study. The arclength (3D distance) and surface distance are compared and very small differences are found between them.

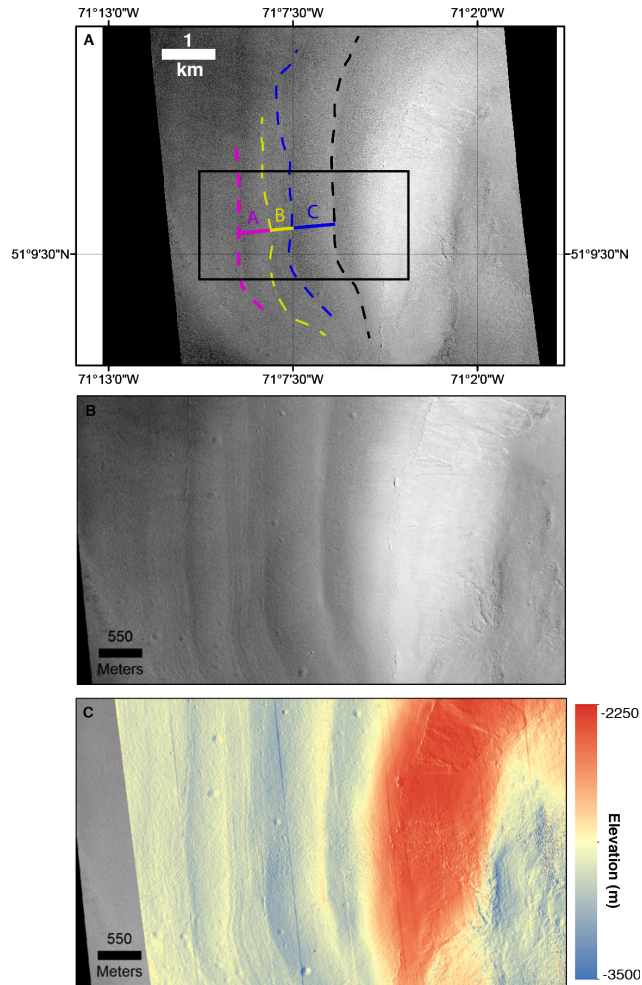


Figure 3.9: Ridges on a debris-covered glacier in Tempe Terra. **(A)** HiRISE image PSP_009341_2315 with mapped ridges and transect measuring inter-ridge distances shown in Table 3.1. Multiple arcuate, transverse ridges are observable on the debris-covered glacier radiating from the massif. The rectangle outlines the bounds of the images below. **(B)** The area within the black rectangle in (A), interpretations removed. **(C)** HiRISE DEM DTEED_009064_2315_009341_2315. Ridges are resolvable in the HiRISE DEM.

Line segment	Surface Distance
A	49.66 m
B	32.17 m
C	64.45 m
D	66.29

Table 3.2: Inter-ridge measurements for the MGF ridges north of Euripus Mons (Figure 3.10, 2.1.C.i.).

the minimum thickness of debris is larger than what is expected based on the model described in Section 2.2. Here, we also find that the difference in arclength measured with the HiRISE DTM and the surface measurement is very small. There are a very limited number of HiRISE DTMs over ridges on martian debris-covered glaciers. Because the difference between the 3D and surface distance is small, however, we use the surface distance as an approximation for the 3D distance in the Euripus Mons case study below.

3.3.2 Euripus Mons Case Study

There are multiple types of ridge morphologies observed on the Euripus Mons debris-covered glacier (Figure 2.1). Here, we check the geometry of the MGF ridges on the northern side (Site 1) and MGC ridges on the western side (Site 2) to determine whether their spacings are consistent with the buckle folding hypothesis.

Site 1 MGF: Table 3.3.2 and Figure 3.10 outline the inter-ridge spacing for the tightly spaced MGF ridges at Euripus Mons. The average ridge distance is 53.1. This yields a range in viscosity ratios $\frac{\mu_1}{\mu_2} = 4 - 430$. Here, we find that the bounds on the debris layer thickness encompass the range of plausible viscosity ratios from Frehner et al. [2015]. Thus, the ridges observed north of Euripus Mons are consistent with a buckle-folding interpretation.

Site 2 MGC: Table 3.3 outlines the inter-ridge spacings for the coarse ridges on the western side of the Euripus Mons debris-covered glacier (Figure 2.1.D.i.). This

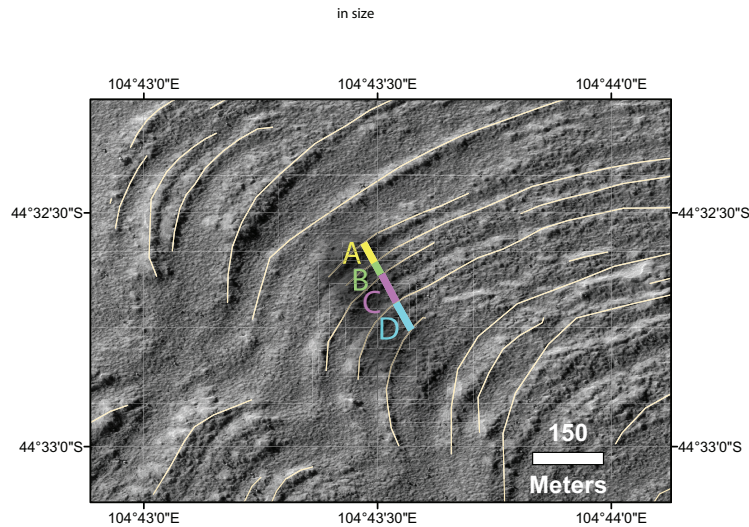


Figure 3.10: Measuring inter-ridge spacing of the “Site 1” MGF ridges on the debris-covered glacier north of Euripus Mons (104.73° , -44.56°).

<u>Line segment</u>	<u>Surface Distance</u>
A	1051.84 m
B	776.21 m
C	850.61 m
D	1124.08

Table 3.3: Inter-ridge measurements for the “Site 2” MGC ridges west of Euripus Mons (Figure 2.1.D.i).

yields an average inter-ridge distance of 950.7 m and a range in the viscosity ratio of $1370-1.4 \times 10^5$. Thus, the viscosity ratio for the maximum thickness of debris is significantly larger than the Frehner et al. [2015] results.

3.3.3 Deuteronilus Mensae Case Study

A HiRISE DTM over a viscous flow feature in Deuteronilus Mensae was available at 38.2° , 45.1° (Figure 3.11). The glacier is too small in the horizontal direction to be resolved by SHARAD, so we cannot relate the basal curvature to the surface textures in this case. Transverse ridges are observed throughout the longitudinal center of

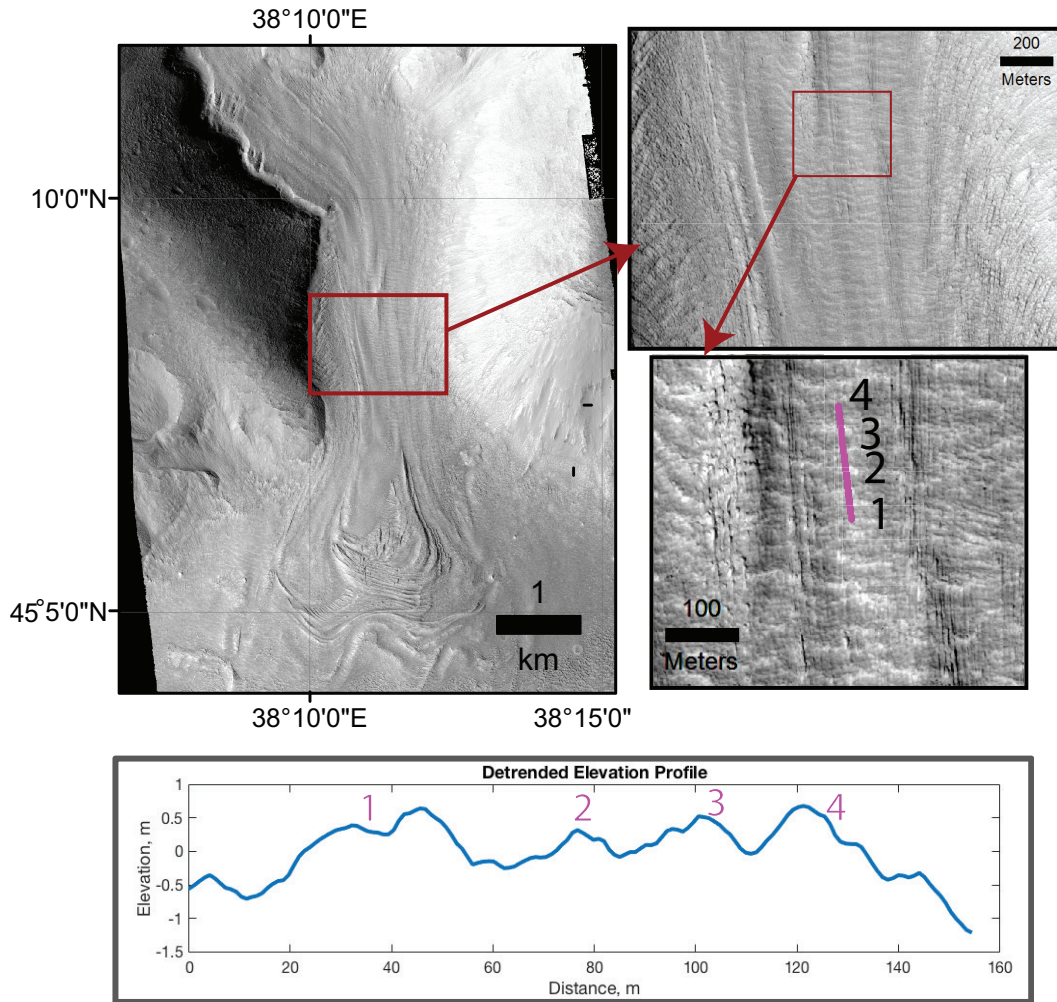


Figure 3.11: HiRISE image ESP_016418_2225 over a viscous flow feature in Deuteronilus Mensae showing surface ridges. The ridges are generally transverse to flow and are short ($\sim 10^1$ - 10^2 m) in the transverse direction. Ridges are resolvable in HiRISE DTM ESP_016418_2225_ESP_017130_2255 and a linearly detrended elevation profile is shown. The arclength measurements along these ridges were used for the buckle folding analysis.

the glacier as it passes through a valley. The average arclength calculated from the detrended elevation profile is 30.8 m. Ridges are short in the transverse-glacier direction with maximum lengths on the order of 10^2 m, and have short transverse wavelengths, sometimes as small as 10% of the total width of the glacier (~ 900 m).

Chapter 4

Discussion

4.1 Formation Mechanisms for Different Ridge Morphologies

Together our results inform interpretation of different morphologies found around Euripus Mons and have implications for understanding the development of debris-covered glacier surfaces for both Earth and Mars. Here we explain possible formation mechanisms for each ridge classification used to map morphologies around Euripus Mons with the aim of trying to identify potential climate signals. We also discuss the results of the terrestrial debris-covered glacier simulations in order to address the alternate hypotheses for the development of englacial debris layers in cold-based glaciers.

Results from the mapping study show that diverse ridge morphologies are found around the Euripus Mons debris-covered glacier complex. Mantling by thin, more recent deposits appears to play a significant role in their exposure, with the broadest and smoothest ridges found on the southern side and the finer, rougher ridges exposed in the northern and western regions. The latitude-dependent mantle is a metres-thick deposit found poleward of $\sim 35^\circ$ in both hemispheres [Kreslavsky

and Head, 2002]. It is thought to be the remnant deposits of widespread ice sheets formed during periods of high martian obliquity. It is currently thought to be undergoing degradation and retreat as midlatitudinal water ice is not stable at Mars' current (25.2°) obliquity [Head et al., 2003]. Because the latitude-dependent mantle has a substantial water ice component, it degrades more rapidly on equator-facing slopes than poleward slopes that are more protected from insolation. It is possible that at Euripus Mons, the latitude-dependent mantle is thicker on the southern, poleward-facing side than the northern side. This could explain the differential morphological expression as one moves from north to south.

The mid-glacier fine (MGF) ridges are observed in areas where the mantle is thinnest. At arclengths ranging from ~ 30 -60 m they have geometries consistent with the buckle folding interpretation. Furthermore, the highly consistent inter-ridge spacings (with rare truncations) and near-constant transverse lengths exhibited by the MGF ridges resembles the morphology of buckle folds observed on terrestrial lava flows (Figure 4.1). Buckle folding has been established as the driving mechanism for the highly regular wavelengths of ridges on terrestrial pahoehoe flows [Fink and Fletcher, 1978]. Given the morphological similarity to pahoehoe buckle folds and the reasonable viscosity ratios estimated from the MGF ridges, it is possible that their predominant formation mechanism is that of buckle folding. If the MGF ridges are indeed buckle folds, then some estimations can be made about the thickness of surficial debris layer. For ridges of longitudinal wavelengths ~ 50 m and the range of plausible viscosity ratios based on terrestrial analogues, the debris layer must be a minimum of 3.3 m thick (Figure 3.8). Because the range of plausible viscosity ratios is based on theoretical maxima as outlined by the terrestrial case, the true thickness is likely to be higher than 3.3 m by this analysis.

This same measure can be applied to the ridges that did not have geometries consistent with the buckle folding hypothesis. For example, the Tempe Terra inter-

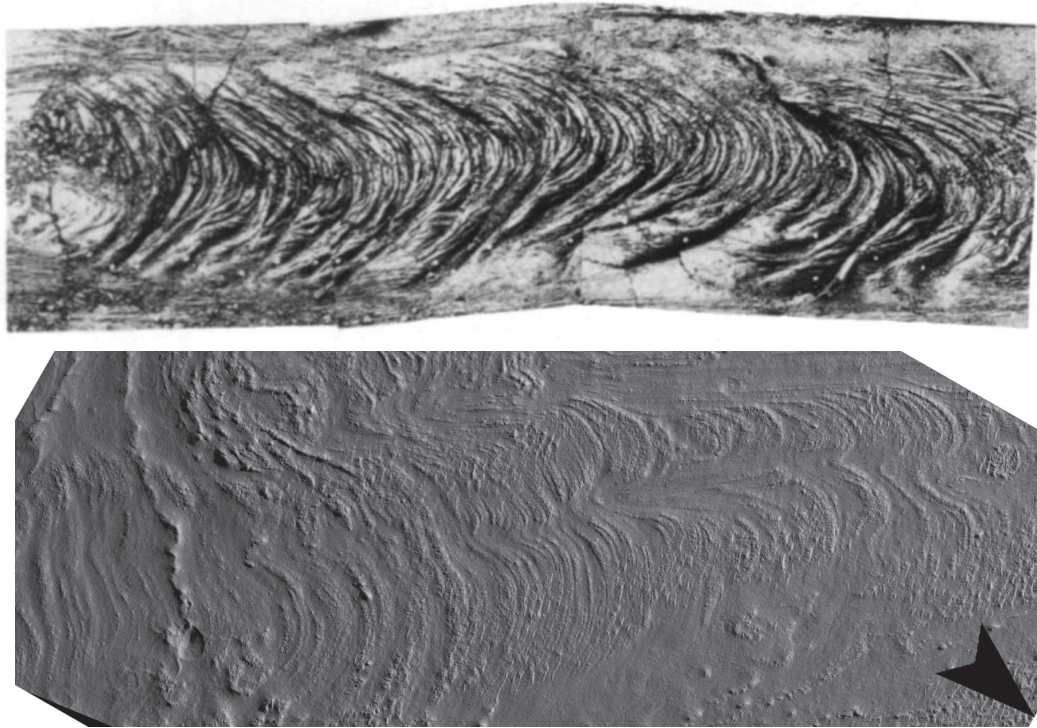


Figure 4.1: Morphological comparison of two-layer buckle fold features and surface ridges on a Euripus Mons debris-covered glacier. **(A)** Buckle folding behaviour on a ropy pahoehoe lava flow. The viscosity contrast between the cooled upper layer and the hot, less viscous lower layer produces consistent and ubiquitous folding of consistent transverse length provided the flow is in a compressive regime. The total longitudinal length is approximately 2.5 m. From Fink and Fletcher [1978]. **(B)** HiRISE image ESP_045334_1350. Ridges on a debris-covered glacier on the northern side of Euripus Mons. Black arrow marks the direction of north. The total longitudinal length is approximately 6 km.

ridge spacing of ~ 580 m would require a debris layer thickness of 37 - 170 m, which is inconsistent with SHARAD results from Holt et al. [2008] and supports our conclusion that the ridges at Tempe Terra are not likely caused by buckle folding.

Even though the dominant formation mechanism for the MGF ridges may be that of buckle folding, it is possible that climatic change has some influence. While the ridges exhibit highly consistent spacing in some areas, other regions exhibit larger and less consistent inter-ridge distances, with wider or narrower peaks, and with varying levels of degradation. Thus, the formation of surface textures in this area is more complex than can be explained by idealized buckle folding alone. Some MGC ridges occur with MGF ridges inbetween them. For example, the MGF ridges in Figure 2.1.C.ii have MGC occurring with them. The MGC ridges west of Euripus Mons (Figure 2.1.D.ii) occur at highly regular intervals and appear to have smooth material inbetween them. The MGC ridges to the north also appear somewhat mantled, but in some areas a higher frequency ridge morphology occurs with it. Where MGC ridges occur without MGF, the inter-ridge spacings are very smooth and exhibit the polygonal, scalloped appearance consistent with the latitude-dependent mantle. This supports the idea that MGC ridges may simply be a more mantled expression of the MGF ridges. If that is the case, then the MGC ridges could represent a longer-wavelength, higher-amplitude mechanism that occurs with the development of MGF.

If the cases where there are no MGF ridges associated with MGC ridges are due to mantling, then the phenomenon of multiple wavelength signals in ridge development must be explained. For the MGF to be hidden by mantling then their peak amplitudes must be smaller than that of MGC. Buckle folding predicts the development of ridges of a consistent spacing and arclength for a given thickness in the debris layer. The arclength measurements for the MGC ridges are far too high to be explained by buckle folding (Figure 3.8). The possibility of shortening is

implausible due to the consistent inter-ridge spacings and general lack of complexity and truncation exhibited by the MGC ridges. Given the lack of other plausible explanations, it is possible that the MGC ridges might be related to climate cycling.

The broad continuous (BC) ridges and the broad non-continuous (BNC) ridges often occur together. It is possible that they are initially formed by the same mechanism but their morphology has been differentially modified due to variable flow histories. The results from the basal surface analysis found that both BC and BNC ridges are associated with slope and profile curvature regimes different from that of the population, and also distinct from each other. The BC ridges preferentially occur in areas of negative profile curvature. This means they tend to occur in extensional regimes and thus compression is likely not a control on their formation. The distribution of basal slope values associated with the BC ridges is also distinct, with a mean (1.2°) slightly lower than that of the population (1.4°). The distribution does not center around a preferred value, however, suggesting that the basal slope is not a strong control on the formation of the BC ridges.

The BNC ridges preferentially occur in areas of positive profile curvature, implying they are most likely to be found in compressive flow regimes. Because they often occur with BC ridges and are of similar scale, it seems likely that they formed by the same mechanism. It is possible that these ridges represent BC ridges that have undergone overthrusting, shortening, and compression due to the decrease in basal slope with distance down-glacier. This is supported by their complex morphology with inconsistent inter-ridge spacings and occasional ridge truncations and also the model results, which produced surface ridges in regions with positive profile curvature.

Accordingly, we interpret the broad continuous ridges as potential climate-related ridges. The basal surface does not seem to have an influence on their formation, they are consistently subparallel to the massif wall, and they are too large to

be explained by buckle folding. Indicators of ridge growth from internal mechanical or rheological processes such as truncations, inconsistent ridge spacing, and overall complexity as expected from compressive shortening are not observed. We propose that the best explanation for how these ridges may form is due to differential accumulation at the headwall with time (Figure 4.2). Preservation and glacial incorporation of atmospherically deposited ice must occur close enough to the headwall that it may be blanketed in debris. Our proposed mechanism describes the expected behaviour resulting from a combination of highly intermittent accumulation cycles and a small accumulation area near the headwall. Following an accumulation event, the ice nearest the headwall advects at greater velocity due to the large driving stresses associated with greater thickness. As this ice advects down-glacier, the differential driving stress causes compression and forms a ridge. The material up-glacier continues moving at a relatively high velocity and material is sapped from the headwall region forming a small depression in the ridge's wake. Thus, the behaviour and preservation of ice nearest the headwall is the dominant control on the long-term morphology and evolution of martian debris-covered glaciers in this model. This behaviour is observed in our modelling results (Figure 3.5.A) and also by observations from imagery shown in Figure 4.3. Our conceptual model predicts that we should observe ridges (1) close to the headwall (2) that run parallel or sub-parallel to the massif headwall and (3) having a depression between the ridge and the headwall. In Figure 4.3, imagery shows martian debris-covered glaciers with surface ridges that meet these criteria. The depression is filled with more recent mantling deposits in all cases.

Figure 4.4 is a profile from a HiRISE DEM over ridges at the Tempe Terra case study site. It shows that the depression observed in imagery is resolvable in elevation data. In the detrended elevation profile there is also an apparent depression inbetween the first and second ridges. This is also expected from our conceptual

model. Ridges further down-glacier from the headwall are not as pronounced in the DEM. This may be due to differential mantling or possible relaxation of ridges as they advect and deform.

It has been hypothesized that cold-based glaciers cannot achieve strain rates high enough to produce thrust faults that can carry basal debris to the surface of a glacier forming englacial debris bands [Mackay et al., 2014, Moore et al., 2010]. Our model results are consistent with this hypothesis in the terrestrial case. The results from the terrestrial debris-covered glacier simulations show diminishing internal structure with decreasing temperatures. The up-glacier dipping bands of high shear strain observed in the temperate terrestrial case are interpreted as thrust faults. Thrust faulting decreases with temperature and does not occur if basal sliding is permitted. All simulations where the glacier was frozen to the bed exhibit a layered strain profile, with a region of high shear strain in the lower glacier and a low-shear, higher-velocity layer moving overtop this region. If the basal surface of the glacier is allowed to slip then the shear strain is lower and thrust faulting is not observed as the sliding accommodates and dissipates any potential build-up of shear stress. In the martian cases where there are thrust faults emerging from the high shear zone in the lower glacier, it is possible that debris from the base may be entrained with it. This would mean there are ways for debris to be entrained in martian glacial ice that do not result from rockfall events during low-accumulation periods. This would add ambiguity to the interpretation of englacial debris bands on Mars, if ever we find any. The lack of thrust faults observed in terrestrial, cold-based simulations supports the idea that englacial debris bands are related to alternating phases of accumulation and ablation in debris-covered glaciers.

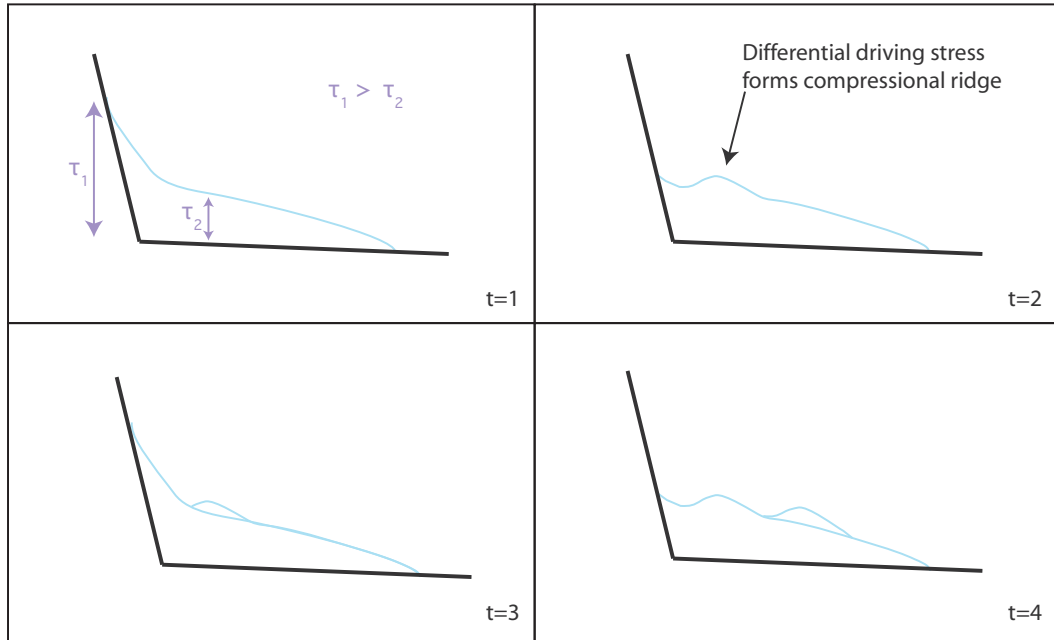


Figure 4.2: A conceptual model for the formation of ridges due to alternating net accumulation and non-accumulation phases. The time steps are denoted by $t = 1$ through 4 in the lower right of each panel. At $t = 1$, accumulation has recently occurred and the driving stress nearest the headwall τ_1 is much higher than the driving stress down-glacier τ_2 . When accumulation stops ($t = 2$) differential driving stress results in a highly compressive regime forming a shortening ridge. At $t = 3$ accumulation starts again and the depression formed at the headwall is filled with new glacial ice. As this advects down-glacier, another ridge forms in the wake of the first one ($t = 4$)

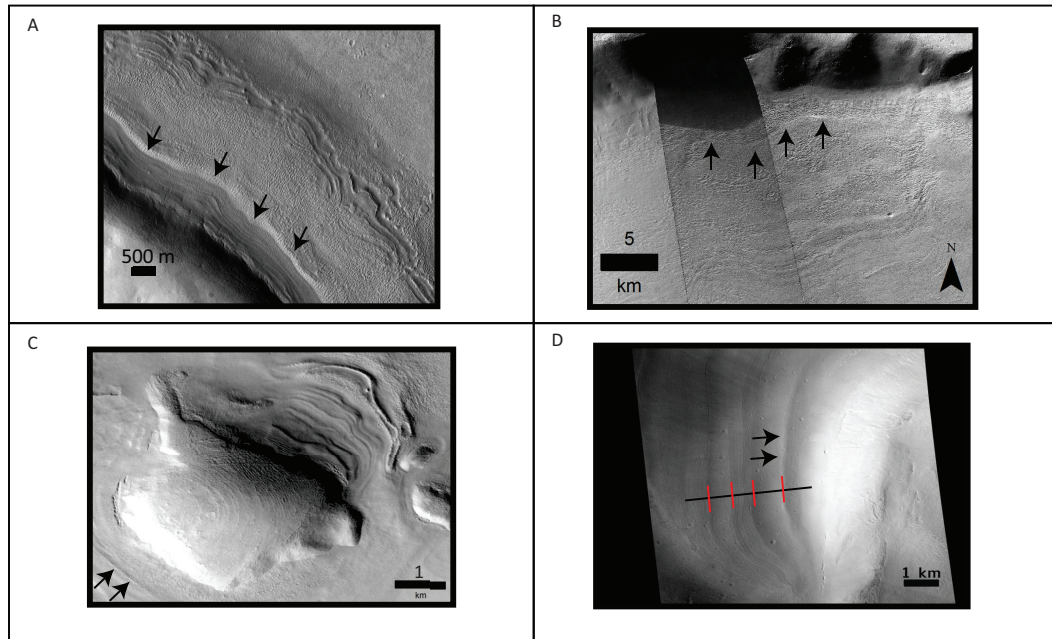


Figure 4.3: **(A)** A debris-covered glacier in Deuteronilus Mensae. A mantle-filled depression is observed nearest the headwall and is bounded by a ridge running subparallel to the massif. **(B)** A subtle ridge on the southern Euripus Mons debris-covered glacier. A shallow, mantle-filled depression is observed between the headwall and the ridge highlighted by the black arrows. **(C)** Ridges on a debris-covered glacier in Protonilus Mensae, centered on 42.80° E, 57.26° N. Ridges to the north are highly pronounced however the area nearest the headwall is obscured by shadows. The southern portions are more heavily mantled, but a subtle ridge is observed on the southern side (arrows) and a depression is observed between it and the headwall. **(D)** Ridges in Tempe Terra (HiRISE image PSP_009341.2315) with the transect for the elevation profile given in Figure 4.4. Vertical red lines mark the interpreted locations of ridges along the elevation profile transect. Centered on 288.8° E, 51.2° N.

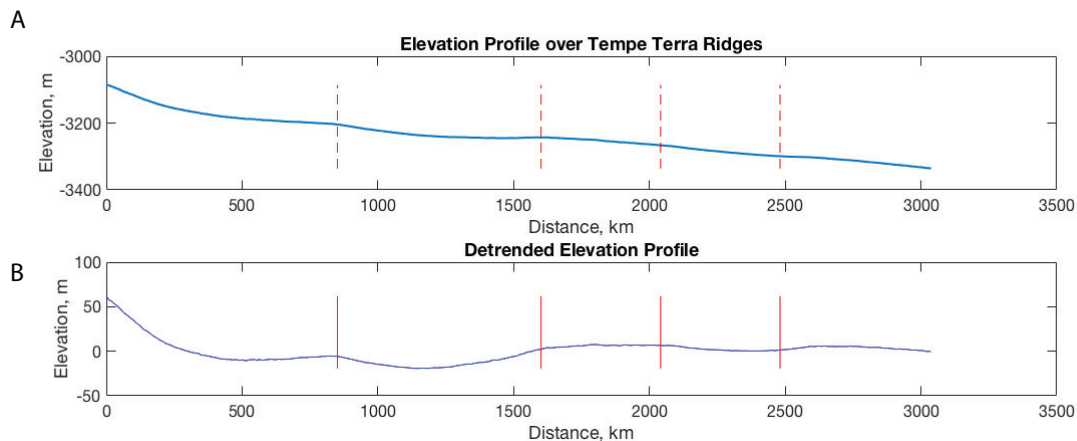


Figure 4.4: **(A)**: Elevation profile from HiRISE DTM 009064_2315_009341_2315 over the transect shown in Figure 4.3.D. Vertical red lines mark the locations of ridges along profile, shown in Figure 4.3.D **(B)**: Detrended elevation profile over Tempe Terra ridges. Depressions ~ 10 -20 m in amplitude are observed around the largest ridges closest to the headwall.

4.2 Limitations of the Buckle Folding Analysis

We identify three main limitations associated with the buckle folding analysis related to both the observations and existing data in the literature. These are (1) the potential mantling of martian ridge amplitudes, (2) the paucity of viscosity ratio measurements for terrestrial debris-covered glaciers and (3) the simplicity of our model for the translation of terrestrially-derived expected viscosity ratios to martian conditions.

It is possible that mantling and in-filling of inter-ridge troughs in Deuteronilus Mensae and Tempe Terra has dampened the true arclength measurement, resulting in a measured arclength value smaller than the actual value. If this is the case then our methods would yield an artificially low viscosity ratio. We thus treat our results as a theoretical minimum value for the true viscosity ratio for a given ridge geometry on Mars. Furthermore, it is important to note that the viscosity ratios found in Frehner et al. [2015] are based on a single terrestrial case. More work is

needed to know if these ratios are truly representative examples for buckle folding on debris-covered glaciers. Additionally, as discussed in Section 2.2, it is difficult to know in what ways the terrestrial viscosity ratios may translate to Mars. Because the viscosity of water ice *increases* dramatically with decreasing temperature and the viscosity of the debris layer *decreases* with decreasing pressure, a *smaller* viscosity ratio $\frac{\mu_1}{\mu_2}$ is expected for martian buckle-folding ridges (See Section 2.2). Thus the maximum ratio for the terrestrial regime is a highly conservative estimate for the maximum viscosity ratio for Mars – if a ridge is too large to be a buckle fold by our determination, it is too large by a fairly generous metric.

Chapter 5

Conclusions

1. Ridges on debris-covered glaciers may be caused by a variety of mechanisms and detailed study is needed to differentiate them. Based on observational studies supported by analytical and numerical models, we have identified criteria by which buckle fold and shortening ridges can be distinguished from ridges associated with climate-driven accumulation patterns. Buckle folding ridges follow an expected geometry based on the overburden thickness, wavelength, and viscosity ratio between the debris layer and the glacial ice. Shortening ridges can be distinguished by the complex morphologies, their context (typically found in the mid-to-lower glacier areas), and compressive basal curvature regimes.
2. A plausible mechanism for the development of climate-related ridges involves intermittent cycles of accumulation and near-headwall compression due to large differential driving stresses. This produces a series of ridges that run parallel to the massif headwall. These ridges do not intersect each other and a depression is expected between the first ridge and the headwall. At Euripus Mons, the largest, smoothest ridges denoted “Broad Continuous” are the most likely to be related to climate based on their geometries and a pattern of

occurrence that is independent of whether the flow regime is extensional or compressional. Ridges similar to this morphology are found in Deuteronilus Mensae, Tempe Terra, and other areas around Eastern Hellas. Further study of these ridges may provide information on martian paleoclimatic changes.

3. The buckle folding hypothesis is a plausible explanation for finely spaced ridges. This possibility could be explored in future work by examining the basal surface underneath the MGF ridges to determine whether the flow regime is consistently compressional. To produce buckle folding ridges along the length of the entire glacier, a consistent decrease in the longitudinal basal slope is expected.
4. We find that thrust faulting is not a likely explanation for englacial debris bands in terrestrial cold-based glaciers as the strain rates are not high enough to produce failure in our simulations. This supports the hypothesis that englacial debris bands demarcate periods of accumulation in terrestrial cold-based glaciers. Thrust faulting may occur in martian debris-covered glaciers as the water ice is much weaker.

References

- Marta Adamuszek, Daniel Walter Schmid, and Marcin Dabrowski. Fold geometry toolbox—automated determination of fold shape, shortening, and material properties. *Journal of Structural Geology*, 33(9):1406–1416, 2011.
- Marta Adamuszek, Daniel W Schmid, and Marcin Dabrowski. Theoretical analysis of large amplitude folding of a single viscous layer. *Journal of Structural Geology*, 48:137–152, 2013.
- Daniel C Berman, David A Crown, and Emily CS Joseph. Formation and mantling ages of lobate debris aprons on Mars: Insights from categorized crater counts. *Planetary and Space Science*, 111:83–99, 2015.
- Maurice Anthony Biot. Theory of folding of stratified viscoelastic media and its implications in tectonics and orogenesis. *Geological Society of America Bulletin*, 72(11):1595–1620, 1961.
- Michael H Carr and Gerald G Schaber. Martian permafrost features. *Journal of Geophysical Research*, 82(28):4039–4054, 1977.
- Frank C Chuang and David A Crown. Surface characteristics and degradational history of debris aprons in the Tempe Terra/Mareotis fossae region of Mars. *Icarus*, 179(1):24–42, 2005.

- Jonathan H Fink and Raymond C Fletcher. Ropy pahoehoe: Surface folding of a viscous fluid. *Journal of Volcanology and Geothermal Research*, 4(1-2):151–170, 1978.
- Caitlyn Florentine, Mark Skidmore, Marvin Speece, Curtis Link, and Colin A Shaw. Geophysical analysis of transverse ridges and internal structure at Lone Peak Rock Glacier, Big Sky, Montana, USA. *Journal of Glaciology*, 60(221):453–462, 2014.
- Marcel Frehner, Anna Hui Mee Ling, and Isabelle Grtner-Roer. Furrow-and-Ridge Morphology on Rockglaciers Explained by Gravity-Driven Buckle Folding: A Case Study From the Murtl Rockglacier (Switzerland): Rockglacier Furrow-and-Ridge Morphology Explained by Buckle Folding. *Permafrost and Periglacial Processes*, 26(1):57–66, January 2015. ISSN 10456740. doi: 10.1002/ppp.1831. URL <http://doi.wiley.com/10.1002/ppp.1831>.
- Kotaro Fukui, Toshio Sone, Jorge Strelin, Cesar Torielli, and Junko Mori. Ground penetrating radar sounding on an active rock glacier on James Ross Island, Antarctic Peninsula region. *Polish Polar Research*, 28(1):13–22, 2007.
- DL Goldsby and DL Kohlstedt. Grain boundary sliding in fine-grained ice. *Scripta Materialia*, 37(9):1399–1406, 1997.
- DL Goldsby and DL Kohlstedt. Superplastic deformation of ice: Experimental observations. *Journal of Geophysical Research*, 106(B6):11017–11030, 2001.
- Peter M Grindrod and Stephen A Fawcett. Possible climate-related signals in high-resolution topography of lobate debris aprons in Tempe Terra, Mars. *Geophysical Research Letters*, 38(19), 2011.
- James W Head, John F Mustard, Mikhail A Kreslavsky, Ralph E Milliken, and David R Marchant. Recent ice ages on Mars. *Nature*, 426(6968):797–802, 2003.

- JW Head, G Neukum, R Jaumann, H Hiesinger, E Hauber, M Carr, Ph Masson, B Foing, H Hoffmann, M Kreslavsky, et al. Tropical to mid-latitude snow and ice accumulation, flow and glaciation on Mars. *Nature*, 434(7031):346–351, 2005.
- John W Holt, Ali Safaeinili, Jeffrey J Plaut, James W Head, Roger J Phillips, Roberto Seu, Scott D Kempf, Prateek Choudhary, Duncan A Young, Nathaniel E Putzig, et al. Radar sounding evidence for buried glaciers in the southern mid-latitudes of Mars. *Science*, 322(5905):1235–1238, 2008.
- Alun Hubbard, Heinz Blatter, Peter Nienow, Douglas Mair, and Bryn Hubbard. Comparison of a three-dimensional model for glacier flow with field data from Haut Glacier d’Arolla, Switzerland. *Journal of Glaciology*, 44(147):368–378, 1998.
- Peter J Hudleston. Structures and fabrics in glacial ice: a review. *Journal of Structural Geology*, 81:1–27, 2015.
- Peter J Hudleston and Susan H Treagus. Information from folds: a review. *Journal of Structural Geology*, 32(12):2042–2071, 2010.
- A. Kääb and M. Weber. Development of transverse ridges on rock glaciers: field measurements and laboratory experiments: Transverse Ridges on Rock Glaciers. *Permafrost and Periglacial Processes*, 15(4):379–391, October 2004. ISSN 10456740. doi: 10.1002/ppp.506. URL <http://doi.wiley.com/10.1002/ppp.506>.
- Martin P Kirkbride and Philip Deline. The formation of supraglacial debris covers by primary dispersal from transverse englacial debris bands. *Earth Surface Processes and Landforms*, 38(15):1779–1792, 2013.
- MA Kreslavsky and JW Head. Mars: Nature and evolution of young latitude-dependent water-ice-rich mantle. *Geophysical Research Letters*, 29(15), 2002.
- Joseph S Levy, James W Head, and David R Marchant. Lineated valley fill and lobate debris apron stratigraphy in Nilosyrtis Mensae, Mars: Evidence for phases of

- glacial modification of the dichotomy boundary. *Journal of Geophysical Research: Planets*, 112(E8), 2007.
- Joseph S Levy, Caleb I Fassett, James W Head, Claire Schwartz, and Jaclyn L Watters. Sequestered glacial ice contribution to the global Martian water budget: Geometric constraints on the volume of remnant, midlatitude debris-covered glaciers. *Journal of Geophysical Research: Planets*, 119(10):2188–2196, 2014.
- Deborah S Loewenherz, Christopher J Lawrence, and Richard L Weaver. On the development of transverse ridges on rock glaciers. *Journal of Glaciology*, 35(121): 383–391, 1989.
- E Logan, L Lavier, E Choi, and E Tan. DynIceSol3D, semi-brittle finite element method for modeling ice failure and dynamics. in prep.
- Baerbel K Lucchitta. Ice and debris in the fretted terrain, Mars. *Journal of Geophysical Research: Solid Earth*, 89(S02), 1984.
- Sean L Mackay and David R Marchant. Obliquity-paced climate change recorded in Antarctic debris-covered glaciers. *Nature Communications*, 8, 2017.
- Sean L Mackay, David R Marchant, Jennifer L Lamp, and James W Head. Cold-based debris-covered glaciers: Evaluating their potential as climate archives through studies of ground-penetrating radar and surface morphology. *Journal of Geophysical Research: Earth Surface*, 119(11):2505–2540, 2014.
- Michael C Malin, James F Bell, Bruce A Cantor, Michael A Caplinger, Wendy M Calvin, R Todd Clancy, Kenneth S Edgett, Lawrence Edwards, Robert M Haberle, Philip B James, et al. Context camera investigation on board the Mars Reconnaissance Orbiter. *Journal of Geophysical Research: Planets*, 112(E5), 2007.
- N Mangold, P Allemand, P Duval, Y Geraud, and P Thomas. Experimental and

- theoretical deformation of ice–rock mixtures: implications on rheology and ice content of Martian permafrost. *Planetary and space science*, 50(4):385–401, 2002.
- Alfred S McEwen, Eric M Eliason, James W Bergstrom, Nathan T Bridges, Candice J Hansen, W Alan Delamere, John A Grant, Virginia C Gulick, Kenneth E Herkenhoff, Laszlo Keszthelyi, et al. Mars reconnaissance orbiter’s high resolution imaging science experiment (hirise). *Journal of Geophysical Research: Planets*, 112(E5), 2007.
- Peter L Moore, Neal R Iverson, and Denis Cohen. Conditions for thrust faulting in a glacier. *Journal of Geophysical Research: Earth Surface*, 115(F2), 2010.
- JF Nye. The mechanics of glacier flow. *Journal of Glaciology*, 2(12):82–93, 1952.
- Reid Parsons and John Holt. Constraints on the formation and properties of a Martian lobate debris apron: Insights from high-resolution topography, SHARAD radar data and a numerical ice flow model. *Journal of Geophysical Research: Planets*, 2016.
- Reid A Parsons, Francis Nimmo, and Hideaki Miyamoto. Constraints on martian lobate debris apron evolution and rheology from numerical modeling of ice flow. *Icarus*, 214(1):246–257, 2011.
- Frank Pattyn, Laura Perichon, A Aschwanden, Beate Breuer, Brigitte De Smedt, Olivier Gagliardini, G Hilmar Gudmundsson, Richard Hindmarsh, A Hubbard, Jesse V Johnson, et al. Benchmark experiments for higher-order and full Stokes ice sheet models (ismip-hom). *The Cryosphere Discussions*, 2(1):111–151, 2008.
- Petersen. New Constraints on Surface Debris Layer Composition for Martian Mid-Latitude Glaciers from SHARAD and HiRISE. March 2017. URL <https://www.hou.usra.edu/meetings/lpsc2017/pdf/2767.pdf>.

- Timothy L Pierce and David A Crown. Morphologic and topographic analyses of debris aprons in the eastern Hellas region, Mars. *Icarus*, 163(1):46–65, 2003.
- Jeffrey J Plaut, Ali Safaeinili, John W Holt, Roger J Phillips, James W Head, Roberto Seu, Nathaniel E Putzig, and Alessandro Frigeri. Radar evidence for ice in lobate debris aprons in the mid-northern latitudes of Mars. *Geophysical research letters*, 36(2), 2009.
- E. Quartini, J. W. Holt, and T. C. Brothers. Internal structure of a lobate debris apron complex in Eastern Hellas: Evidence for multiple mid-latitude glaciations on Mars. In *42nd Lunar and Planetary Science Conference*, page Abstract #2470, Houston, 2011. Lunar and Planetary Institute. URL <http://www.lpi.usra.edu/meetings/lpsc2011/pdf/2470.pdf>.
- Roberto Seu, Roger J Phillips, Daniela Biccari, Roberto Orosei, Arturo Masdea, Giovanni Picardi, Ali Safaeinili, Bruce A Campbell, Jeffrey J Plaut, Lucia Marinangeli, et al. SHARAD sounding radar on the Mars Reconnaissance Orbiter. *Journal of Geophysical Research: Planets*, 112(E5), 2007.
- David E Smith, Maria T Zuber, Herbert V Frey, James B Garvin, James W Head, Duane O Muhleman, Gordon H Pettengill, Roger J Phillips, Sean C Solomon, H Jay Zwally, et al. Mars Orbiter Laser Altimeter: Experiment summary after the first year of global mapping of Mars. *Journal of Geophysical Research: Planets*, 106(E10):23689–23722, 2001.
- Sarah M Springman, Lukas U Arenson, Yuko Yamamoto, Hansruedi Maurer, Andrew Kos, Thomas Buchli, and Guido Derungs. Multidisciplinary investigations on three rock glaciers in the Swiss Alps: legacies and future perspectives. *Geografiska Annaler: Series A, Physical Geography*, 94(2):215–243, 2012.

- Steven W Squyres. Martian fretted terrain: Flow of erosional debris. *Icarus*, 34(3): 600–613, 1978.
- Steven W Squyres. The distribution of lobate debris aprons and similar flows on Mars. *Journal of Geophysical Research: Solid Earth*, 84(B14):8087–8096, 1979.
- Steven W Squyres and Michael H Carr. Geomorphic evidence for the distribution of ground ice on Mars. *Science*, 231(4735):249–252, 1986.
- Tuan Ta, Kyoshin Choo, Eh Tan, Byunghyun Jang, and Eunseo Choi. Accelerating DynEarthSol3D on tightly coupled CPU–GPU heterogeneous processors. *Computers & Geosciences*, 79:27–37, 2015.
- Clyde Wahrhaftig and Allan Cox. Rock glaciers in the Alaska range. *Geological Society of America Bulletin*, 70(4):383–436, 1959.